**PRODUCTION AND CHARACTERIZATION
OF
FEMTOSECOND-LASER-INDUCED
AIR PLASMA**

THESIS

David R. Armbruster, Captain, USAF

AFIT/GAP/ENP/08-M01

**DEPARTMENT OF THE AIR FORCE
AIR UNIVERSITY**

AIR FORCE INSTITUTE OF TECHNOLOGY

Wright-Patterson Air Force Base, Ohio

PRODUCTION AND CHARACTERIZATION OF FEMTOSECOND-LASER-
INDUCED AIR PLASMA

THESIS

Presented to the Faculty

Department of Engineering Physics

Graduate School of Engineering and Management

Air Force Institute of Technology

Air University

Air Education and Training Command

In Partial Fulfillment of the Requirements for the

Degree of Master of Science in Applied Physics

David R. Armbruster, B.S.

Captain, USAF

March 2008

AFIT/GAP/ENP/08-M01

PRODUCTION AND CHARACTERIZATION OF FEMTOSECOND-LASER-
INDUCED AIR PLASMA

David R. Armbruster, BS

Captain, USAF

Approved:

//SIGNED//_____   _____
Matthew J. Bohn (Chairman)   Date

//SIGNED//_____   _____
Jack E. McCrae (Member)   Date

//SIGNED//_____   _____
Jason A. Diebel (Member)   Date

//SIGNED//_____   _____
Douglas T. Petkie (Member)   Date

ABSTRACT

The purpose of this research was to produce, characterize, and optimize laser-induced air plasma as a preliminary step in using the plasma as a source of terahertz radiation. An 800 nanometer, 50 femtosecond, 0.75 Watt, pulsed Ti:Sapphire laser system was used as the source infrared beam. A beam expander was used to expand the beam to a diameter of approximately 6.5 mm, and the beam was focused through a 25 mm focal length achromatic lens to produce laser-induced plasma in ambient air. A 40 kHz ultrasonic transducer was used to detect the plasma. A second harmonic generation crystal was placed within the beam expander to generate 400 nm blue light, enabling production of THz in the plasma via four wave mixing; a third-order nonlinear process. While plasma-produced THz was not detected, all the preliminary groundwork was accomplished, including full characterization of the plasma, blue light, and alignment of the system to generate and detect THz. The electro-optic detection apparatus was assembled, aligned and used to successfully detect a diagnostic THz signal.

TABLE OF CONTENTS

Page

Abstract iv

Acknowledgments..v

Table of Contents vi

List of Figures vii

Introduction..1

Background 3

2.1 Terahertz 3

2.2 Ultrashort Pulse Propagation 5

2.3 Four Wave Mixing, Plasma and Terahertz 11

III. Equipment 14

3.1 Verdi-Pumped Femtosecond Laser System..14

3.2 Frequency-Resolved Optical Grating (FROG) 15

3.3 Nirvana Autobalanced Photodetector 17

IV. Experimental Results and Analysis 18

Conclusion 44

Bibliography 45

LIST OF FIGURES

PRODUCTION AND CHARACTERIZATION OF FEMTOSECOND-LASER-INDUCED AIR PLASMA

INTRODUCTION

Imagine a portable device that can look through the paint on an airframe to inspect for metal fatigue, or find voids and imperfections inside or beneath space shuttle tiles. Picture an airport terminal equipped with an unobtrusive scanner capable of detecting banned items or hazardous substances hidden under clothing, or perhaps a medical scanner that can detect cancerous cells before they are detectable by other means, all without the use of harmful ionizing radiation. These are but a few of the many possible applications of terahertz (THz) based systems.

THz is of interest for these applications for many reasons. Due to its low photon energies (~4 meV), THz radiation is non-ionizing, leading to interest for biological imaging. Compared to X-rays, THz radiation is relatively easy to focus, leading to wavelength-limited image resolution. Water is a strong absorber of THz radiation, which limits transmission through the atmosphere but makes THz a good detector of water levels in materials. This strong atmospheric absorption also makes THz an interesting possibility for satellite-to-satellite communications, because such signals would not be detectable at ground level. THz wavelengths are well matched to the vibrational energies of many chemical structures, leading to characteristic absorption patterns for many

organic crystals (like those found in explosives) and bacterial compounds (such as anthrax) [1]. Hence, these materials have a THz "fingerprint," another reason for choosing THz as the basis for detection systems.

This thesis investigates one of the basic building blocks necessary for such future systems: a source of THz radiation. In this research, the goal was to produce THz via a four-wave mixing process (FWM) in laser-induced air plasma. An 800 nm femtosecond ($1fs = 10^{-15}s$) pulsed laser system generates the infrared beam (IR) used to produce air plasma via a variety of optical components. A second-harmonic generation (SHG) crystal is added to the optical train to provide the frequency-doubled (400 nm blue) light necessary to the THz production. Several optical configurations are investigated in an attempt to produce and detect the plasma generated THz. In the course of this research, characteristics of the prerequisite components were established and optimized. While plasma generated THz was not detected, an upper limit was determined for the intensity of the plasma generated THz produced by this system, and the appropriateness of the electro-optic technique for detecting THz is proven.

Chapter II of this thesis will provide the reader with the background information required to understand the challenges and goals of this research effort. Chapter III will provide a detailed description of the equipment used throughout this research. Chapter IV will present the experiments and findings obtained from this research, along with analysis of the results. In conclusion, Chapter V will summarize the progress made during this research and make some conjecture regarding the road ahead.

The first mode-locked pulse laser was demonstrated in 1964 and produced nanosecond pulses [2]. By 1987, pulses as short as 6 fs were achieved [3]. Commercial laser systems are readily available today which routinely produce sub-100 fs pulses. These pulsed laser systems are finding application in a variety of fields, and as pulses become even shorter, it becomes possible to study events on an increasingly shorter time scale. For example, the isomerization of rhodopsin, a key process in human vision, occurs on a timescale of approximately 200 fs [4]. During the last 20 years, advances in continuous wave (CW) and ultrafast laser sources have enabled new research into nonlinear optical methods of conversion from visible and near-IR frequencies into the THz regime.

2.1 TERAHERTZ

The THz portion of the electromagnetic spectrum, from roughly 10 to 1000 micrometer wavelengths, lies between the microwave region and the infrared region. This region is a "gap" which lies above microwave frequencies (generated by carrier transport based electronic devices) and below infrared frequencies (generated by quantum-transition based photonic devices) as seen in Figure 1. As a result, producing THz radiation has historically been either very difficult or very expensive (or both). While sources such as the backward wave oscillator or the free electron laser are capable of producing THz radiation, it is only in the last 20 years that advances in ultrafast laser sources have enabled new research into nonlinear optical methods of conversion from
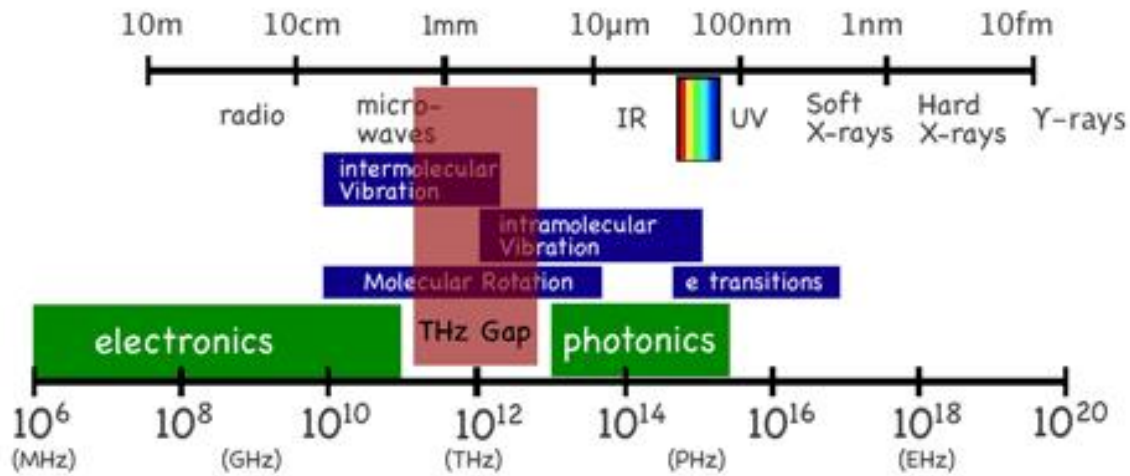
Figure 1. The electromagnetic spectrum [5].

visible and near-IR into THz. For an imaging or detection system, a THz source must possess a high repetition rate to enable fast scan rates, and deliver sufficient average power to achieve a good signal to noise ratio. Nonlinear optical methods make possible a THz radiation source of sufficient power to be of interest in many possible applications. As the lasers that are used to produce these THz waves progress to shorter pulses and higher powers, the peak intensities of the pulses grow very large indeed. For example, in 1996 Lawrence Livermore National Lab's Petawatt Laser produced a 440 fs pulse that reached a record-setting 1.25 PW ($1PW = 1 \cdot 10^{15} W$) of peak power, while the Hercules laser at University of Michigan's Center for Ultrafast Optical Science holds the world record for on-target laser intensity at $10^{22} W/cm^2$. Pulsed lasers delivering even a fraction of this power are more than powerful enough to cause non-linear optical effects to occur even in media that are typically considered linear, such as ambient air. Some of the non-

linear effects applicable to pulsed lasers are Self-Phase Modulation (SPM), the optical

Kerr effect, Raman scattering, and four wave mixing. A complete study of these subjects

is well beyond the scope of this thesis. However, there are some key concepts in the

linear and nonlinear propagation of short pulses that should be introduced.

2.2 ULTRASHORT PULSE PROPAGATION

Fundamentally, an ultrashort light pulse can be described as a group of optical

cycles contained within a pulse envelope, as shown in Figure 2. It should be noted that

the Gaussian pulse shape is commonly used to make the mathematics less difficult, but

the pulse envelope is typically not a Gaussian [6]. The laser system used in this research,
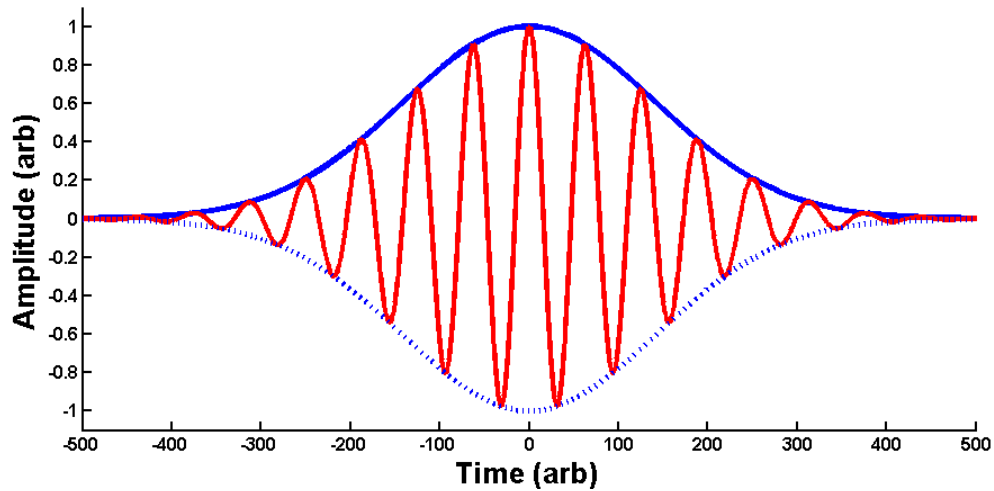
for example, approximates a sech pulse.

Figure 2. A Gaussian pulse

Mathematically, a Gaussian pulse can be described by a collection of exponential

functions, as shown in Equation (2.1).

5

$$\tilde{E}^+(t) = A_0 e^{-\alpha t^2} \cdot e^{i\varphi_0} \cdot e^{i\varphi(t)} \cdot e^{i\omega_l t} \qquad (2.1)$$

The pulse envelope is described by the real (Gaussian in this case) component, $A_0 e^{-\alpha t^2}$.

The frequency of the group of optical cycles contained within the pulse envelope, also

known as the carrier frequency, is given by ω_l. The remaining terms describe the phase

of the pulse, where φ_0 is the initial phase and $\varphi(t)$ is the phase as a function of time. The

total instantaneous phase of the pulse is then given by $\varphi_0 + \varphi(t)$. The instantaneous

frequency, which is the rate at which the total phase propagates forward in time, is then

given by the time derivative of the instantaneous phase, $\frac{\partial}{\partial t}\varphi(t)$. This expression

describes how the instantaneous frequency varies in time, and this variation is referred to

as the "chirp" of the pulse. For instance, if $\frac{\partial}{\partial t}\varphi(t)$ is linear in time (e.g. $2at + b$), then the

component frequencies of the pulse are increasing (or decreasing) in time, and the pulse

has a linear upchirp (or downchirp). A linearly upchirped pulse and the corresponding

Gaussian pulse envelope are plotted in Figure 3. The sign of the second derivative,

$\frac{\partial^2}{\partial t^2}\varphi(t)$, tells us if the pulse is upchirped (positive second derivative) or downchirped

(negative second derivative). Interestingly, if $\frac{\partial^2}{\partial t^2}\varphi(t)$ is a constant, then the time-

dependent phase of the pulse $\varphi(t)$ must be a quadratic function in time, of the form

$a \cdot t^2 + b \cdot t + c$. It is important to note that a chirped pulse will have an increased time
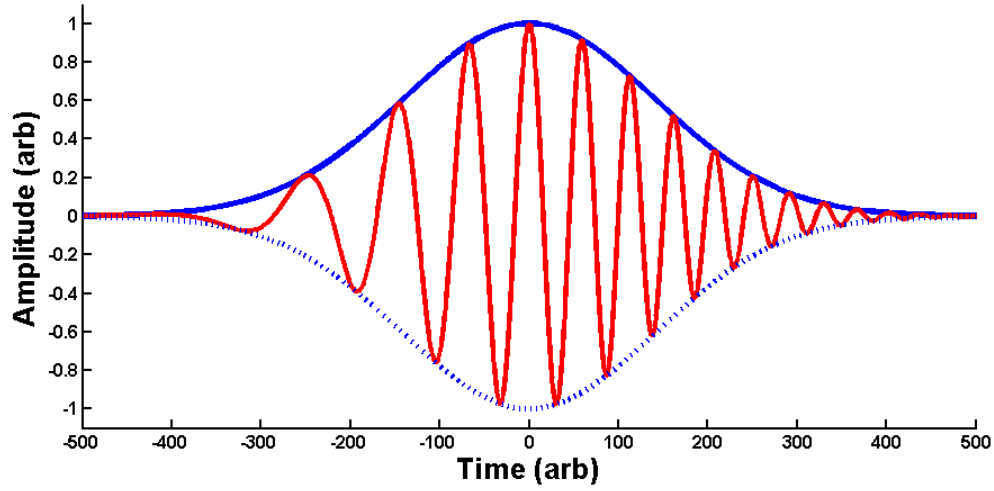
Figure 3. An upchirped Gaussian pulse

bandwidth product as compared to an unchirped pulse of the same shape, and is therefore

wider in time than its transform limit. A useful result of this is that if a chirped pulse is

sent through a medium in which different frequencies propagate at different speeds, the

chirp can either be enhanced or reduced, thus expanding or compressing the pulse[6]. We

rely on this behavior in most of the experiments presented in this thesis.

The relationship between temporal pulse width and frequency bandwidth is seen

in the Fourier relationship between time and frequency, which requires that as a pulse

shortens in time, its frequency bandwidth increases. We can also use Heisenberg's

uncertainty principle to explain this observation. Starting from the uncertainty principle,

$\Delta t \cdot \Delta E \geq h$ [7], and using the definition $E = h \cdot \nu$, we see that there is a relation between

time and frequency given by $\Delta t \cdot \Delta \nu \geq 1$. As Verdeyen points out in [7], this value (1, ½,

etc), depends on how Δt and $\Delta \nu$ are defined. Defining a parameter such as Δt becomes

difficult when considering very short pulses, and defining Δv is difficult when describing just a few optical cycles. Fortunately, we can define a related quantity, the time-bandwidth product (labeled c_B in [6]) in a similar fashion:

$$\Delta v \cdot \tau_p \geq c_B \qquad (2.2)$$

where τ_p is the FWHM pulse duration and Δv is the FWHM bandwidth in frequency. We see that the basic idea of the uncertainty principle is retained: the product of the pulse "size" in time and frequency is equal to some constant with a lower bound. A bandwidth-limited or transform-limited pulse is defined as a pulse that has a time-bandwidth product equal to the minimum possible c_B. This value differs for different pulse shapes, but common values are 0.441 for a Gaussian pulse and 0.315 for a sech pulse [6]. Equation (2.2) may be re-written to yield the spectral bandwidth $\Delta \lambda$:

$$\frac{c_B \cdot \lambda^2}{c \cdot \tau_p} \leq \Delta \lambda \qquad (2.3)$$

where c is the speed of light (~300 nm/fs) and λ is the central wavelength of the laser. For a bandwidth-limited pulse, the relationships in Equations (2.2) and (2.3) are equalities. For example, a bandwidth-limited sech pulse of 50 fs and a central wavelength of 800 nm has a spectral bandwidth (at FWHM) of approximately 13 nm, corresponding to $6.3 \cdot 10^{12} Hz$ (6.3 THz) in frequency bandwidth.

To investigate how these pulses travel, we return to basic electromagnetic theory. The propagation constant k for a wave traveling in a medium is defined as follows,

$$k = \frac{2\pi v}{c} n(\lambda) \qquad (2.4)$$

where c is speed of light and $n(\lambda)$ is the index refraction as a function of wavelength. The group of optical cycles making up the pulse travels at the phase velocity, while the pulse itself (the entire envelope) travels at the group velocity. The phase velocity is given by $v_p = \dfrac{c}{n(\lambda)}$, and the group velocity is defined in Equation (2.5).

$$\frac{1}{v_g} = \frac{\partial k}{\partial \omega} = \frac{n}{c} - \frac{\lambda}{c}\frac{dn}{d\lambda} \tag{2.5}$$

As shown in Equation (2.5), the group velocity is frequency dependent. Thus as the pulse travels, either the higher (blue) frequencies will pull ahead of the lower (red) frequencies, or the red will "catch up" as the higher frequencies are slowed by the medium. This behavior is known as Group Velocity Dispersion (GVD). For an upchirped pulse, positive GVD stretches the pulse in time, while negative GVD compresses the pulse. A key aspect of GVD is that it is a linear effect, and therefore obeys time reversal. The practical impact is that a laser cavity can be designed with a specific total amount of positive or negative GVD, which must be controlled for a mode-locked laser to operate. For example, in a Cr:LiSAF cavity as pictured in Figure 4 (a), the three mirrors (M) can be chosen with a specific amount of negative GVD, thanks to the availability of specialized "double-chirped" mirrors which reflect red wavelengths sooner than blue, as seen in Figure 4 (b). The Cr:LiSAF crystal itself has positive GVD, so by choosing the mirrors carefully the exact amount of total GVD in the cavity is specified.
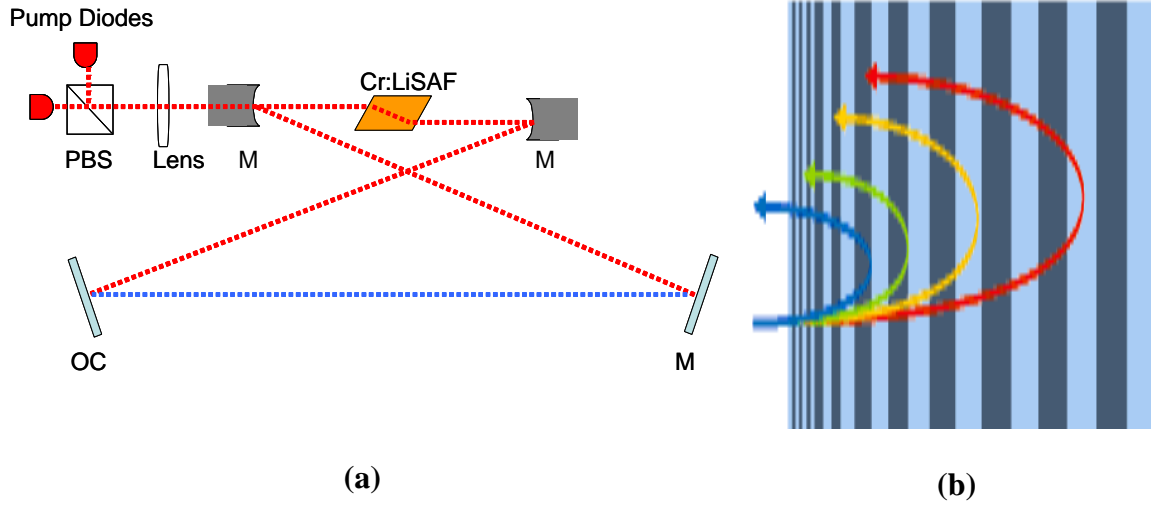
(a)　　　　　　　　　　　　　　　　　**(b)**

Figure 4. (a) Diode-pumped Cr:LiSAF cavity and **(b)** "double-chirped" mirror

Again returning to basic electromagnetic theory, we have the following

expressions, arising from Maxwell's Equations for a nonmagnetic neutral dielectric

medium, the definition of the magnetic field vector for non-magnetic media, and the

definition of the electric displacement vector:

$$\nabla \times E = -\mu_0 \frac{\partial H}{\partial t} \tag{2.6}$$

$$B = \mu_0 H \tag{2.7}$$

$$D = \varepsilon_0 E + P \tag{2.8}$$

where E is the electric field vector, μ_0 is the permeability of free space, H is the

magnetic field, B is the magnetic flux density, D is the electric displacement, ε_0 is the

permittivity of free space, and P is the polarization density [8]. By taking the curl of E,

along with the definition of the speed of light in a vacuum, $\frac{1}{\sqrt{\mu_0 \varepsilon_0}} = c$, and using

$\nabla \cdot E = 0$ for transverse waves, we arrive at the one-dimensional inhomogeneous wave

equation:

$$\nabla^2 E = \frac{1}{c^2}\frac{\partial^2 E}{\partial t^2} = \frac{1}{\varepsilon_0 c^2}\frac{\partial^2 P}{\partial t^2} \qquad\qquad (2.9)$$

The polarization density P can be expressed as a Taylor series in the applied field,

$$P = \varepsilon_0 \chi_1 E + \chi_2 E^2 + \chi_3 E^3 + \cdots \qquad\qquad (2.10)$$

where χ_1, χ_2 & χ_3 are the linear, second-order and third-order optical susceptibilities of

the medium [9]. As seen in Equation (2.9), the polarization affects the propagation of the

electric field through a medium, and Equation (2.10) shows that as the strength of the

electric field increases, the higher order terms become more important to the polarization.

For a relatively weak electric field, the polarization is linear and the response of the

medium is simply the index of refraction. For stronger electric fields, the second and third

order terms contribute different effects to the response of the medium. Second-order

nonlinearity produces effects including frequency doubling or second-harmonic

generation (SHG), sum- and difference-frequency generation, and parametric

amplification and oscillation [9]. The third-order nonlinearity drives effects mentioned

earlier, including Self-Phase Modulation (SPM), the optical Kerr effect, Raman

scattering, and four wave mixing. The effect most important to this research is the four

wave mixing process.

2.3 FOUR WAVE MIXING, PLASMA AND TERAHERTZ

Four wave mixing (FWM), simply defined, is the process in which one frequency

is created from the summation of three other (not necessarily unique) frequencies.

Several examples of FWM are shown below:

$$\omega_4 = \omega_1 + \omega_2 + \omega_3$$
$$\omega_4 = \omega_1 + \omega_2 - \omega_3$$
$$\omega_4 = \omega_1 + \omega_1 + \omega_1 = 3\omega_1$$

In this research, we will be using 400 nm blue, 800 nm IR, and 800 nm IR again to produce THz waves. When put into angular frequencies, we see that this process is described by

$$\omega_{\text{BLUE}} - 2 \cdot \omega_{IR} = \omega_{THz} \tag{2.11}$$

Blue light at 400 nm has angular frequency $\omega_{Blue} \cong 2\pi \cdot 7.5 \cdot 10^{14} \, Hz$, and the 800 nm IR

beam has angular frequency $\omega_{IR} \cong 2\pi \cdot 3.7 \cdot 10^{14} \, Hz$, resulting in an ω_4 of $\sim 2\pi \cdot 1 \cdot 10^{13} \, Hz$,

or 10 THz. A key assumption in this research is that FWM is the primary mechanism generating THz in laser-induced air plasma [10-13]. As we saw earlier, FWM is a nonlinear effect, indicating that a high applied field is required for the process to occur. With this in mind, we look at what happens to the short pulse as it propagates through an optical component such as a glass lens. Using simple equations for spot size Δl and peak power Pp,

$$\Delta l = 1.22 \frac{f \lambda}{d} \tag{2.12}$$

$$P_p = \frac{E_p}{\tau} \tag{2.13}$$

where f is the focal length of the lens, λ is the wavelength, d is the beam waist [14], τ is

the pulse width in seconds, and E_p is the peak pulse energy in Joules. For example, a

50 fs pulse with $8 \, \mu J$ peak energy has a peak power of 160 MW. At a wavelength of

800 nm, with a beam diameter of 2.7 mm and a 25 mm focal length lens, $P_p \Big/ \pi \left(\frac{\Delta l}{2} \right)^2$

yields a power density at the focal point of approximately 2.5×10^{14} W/cm^2. The commonly accepted power threshold to produce plasma in air is 1.5×10^{14} W/cm^2, so we are clearly producing sufficient power to see laser-induced air plasma and create nonlinear effects such as four wave mixing. While plasma alone will radiate THz waves, it does so as a point source radiating in all directions. For a weak plasma, this results in THz radiation of too low an intensity to be useful. However, the FWM process produces THz waves in the direction of beam propagation and delivers the highest peak THz field.

It should be noted that in the development of these results from Maxwell's equations, the common assumptions are made: no free charge and no current in a uniform non-magnetic media. These assumptions are not necessarily valid once a plasma is formed. However, the further assumption is made that these approximations will be "close enough" to enable us to press on and achieve reasonable results.

III. EQUIPMENT

3.1 VERDI-PUMPED FEMTOSECOND LASER SYSTEM

All of the experiments in this research effort were performed using a Coherent fs-pulsed laser system. This system consists of a Coherent (MIRA 900) titanium sapphire (Ti:Sapphire) modelocked oscillator, a Coherent regenerative amplifier (RegA 9000), a compression/expansion module, and a frequency-doubled 532 nm Nd:YVO4 pump laser (Coherent Verdi V18). A schematic is shown in Figure 5.
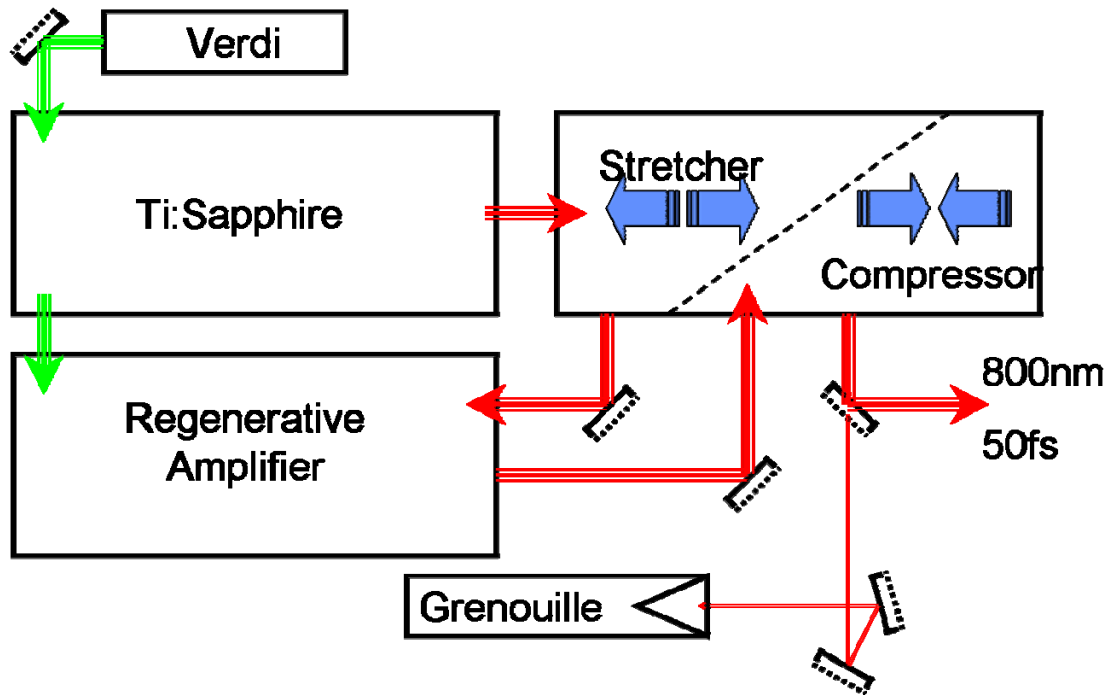

Figure 5. Schematic of Coherent fs-pulsed laser system with Grenouille

The 18 W Verdi beam pumps the 76 MHz MIRA, which produces 50 fs pulses at a central wavelength of 800 nm. The pulses then undergo Chirped Pulse Amplification, beginning with the expansion module. Each pulse is stretched out in duration to

14

approximately 200 ps, which greatly reduces the peak power. Next, the pulse is directed

into the RegA (also pumped by the Verdi), where this long duration pulse is amplified in

the course of approximately 20 round trips. While the RegA is tunable anywhere between

40 and 300 kHz, the majority of this research was conducted at a repetition rate of 100

kHz. After the RegA, the pulse is re-compressed, resulting in a beam comprised of 50 fs

pulses at the repetition rate of the RegA, with a central wavelength of 800 nm, a beam

diameter of 2.68±.02 mm, and a typical average power of 750 mW. The pulse peak

energy is then approximately .750 W/100 kHz, or about 8 μJ. While each 8 μJ pulse is of

fairly low energy, the peak power of the laser is quite high: $8\mu J / 50 fs = 1.6 \cdot 10^8 W$. The

first turning mirror (after the compressor) has a reflectivity of 99.9%, which provides a

diagnostic beam of .1% of the system's output for beam characterization equipment such

as the Grenouille.

3.2 FREQUENCY-RESOLVED OPTICAL GRATING (FROG)

In measuring ultrashort pulses, the main drawback of autocorrelation is the need

to use the pulse to measure the pulse. This presents difficulties because the details of

pulse structure become washed out in the autocorrelation. An improvement to

autocorrelation was presented when Kane and Trebino introduced a short pulse

measurement technique known as frequency resolved optical gating or FROG [15] in

1993. The basic design of an SHG FROG is shown in Figure 6. The Grenouille, a device

based on the FROG technique, spectrally resolves temporal slices of a pulse. The

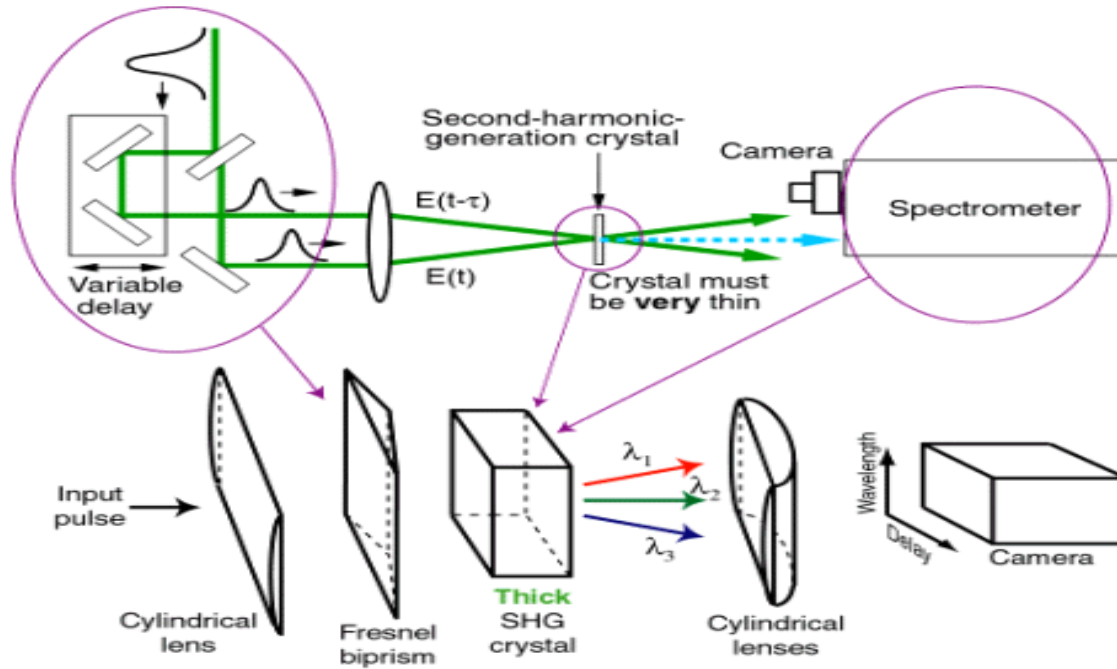Grenouille is a simplified version of an SHG FROG, using a thick SHG crystal and

Figure 6. Typical FROG and Grenouille diagram [17].

various optical components to simplify the system by eliminating the need for an optical delay line. When paired with the QuickFrog software package, ultrashort laser pulses can be measured by the device and viewed in real time on the computer screen. The Grenouille measures both spatial and temporal parameters, using an SHG crystal and CCD camera to give instantaneous feedback on wavelength, pulse width, intensity, phase vs. time, spatial profile, spatial chirp and pulse-front tilt [16]. Unlike an autocorrelator, the Grenouille measures the actual laser pulse width in addition to the FWHM value for τ. Although it does measure spatial chirp, one drawback to the Grenouille is that is does not provide any information on the temporal chirp of the pulse. Another drawback is that the sign of the measured chirp is ambiguous.

16

3.3 NIRVANA AUTOBALANCED PHOTODETECTOR

The New Focus Nirvana autobalanced photoreceiver is also worth mention here. The autobalanced detector simply compares intensities of a signal beam and a reference beam, and outputs a voltage based on the difference in intensities. A simple example of this process is shown in Figure 7. This figure depicts a simplified setup for electro-optic (EO) detection of a THz signal using the autobalanced photoreceiver. In Figure 7 (a), the IR beam passes through the EO crystal and then through a polarizing beam splitter (PBS), splitting the beam into vertical and horizontal components. These component beams are aligned into the Nirvana, which is then tuned until the signal (voltage out) is zero. Now the detector reads zero as long as the intensities of the vertical and horizontal component beams are equal. In Figure 7 (b), the THz source is turned on, and THz radiation arrives at the EO crystal along with the IR beam. Since the IR frequency is much greater than the THz frequency, the EO crystal sees the THz signal as a DC applied field. An EO crystal is birefringent, so with an applied field the crystal rotates the polarization of the IR beam. This changes the horizontal and vertical component beam intensities, leading to a voltage out of the Nirvana due solely to the presence of the THz source.
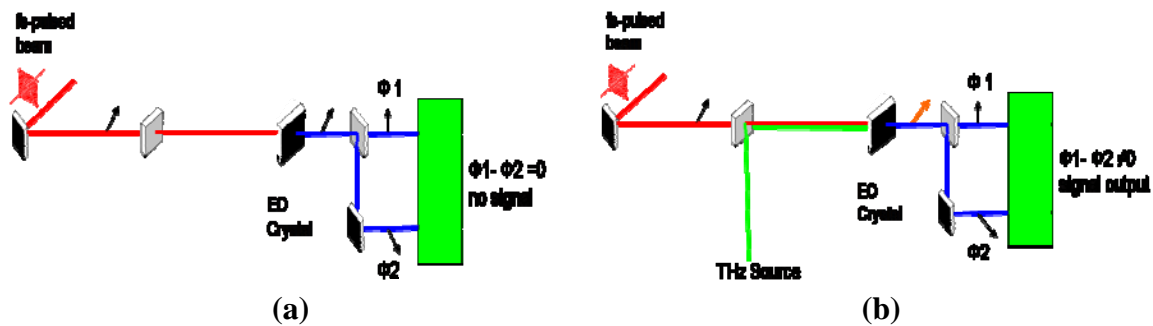

(a)   **(b)**

Figure 7. (a) Nirvana with no signal output and **(b)** Nirvana signal output due to THz

IV. EXPERIMENTAL RESULTS AND ANALYSIS

This research successfully produced and characterized femtosecond-laser-induced plasma in ambient air. In addition, the components of plasma production were characterized, including blue light produced by an SHG crystal and a safe, reliable method to "see" the plasma produced. All of the experiments in this research effort used the beam produced by the Coherent fs-pulsed system described in Chapter III. For simplicity, the apparatus sketches presented will only detail the optical component train and detector changes required by the different experiments.

Laser performance was monitored in several ways. Initially an Ocean Optics spectrometer was used to determine the spectrum of the beam. After calibration of the spectrometer using an argon light source (7635.1 Å), the central wavelength of the beam spectrum was measured at 7877.1 Å. The FWHM spectral bandwidth was measured to be 15.3 ± 0.4 nm, which for a typical pulse width of 50 fs yields a time bandwidth product of .37 from Equations (2.2) and (2.3). This number matches exactly with the typical Grenouille value of .37 seen over the course of this research. As we can see, this value is larger than the bandwidth limited value of .315, which is explained by the presence of chirp in the pulse.

The diagnostic beam (the .1% that passes through the first turning mirror) is directed via two aiming mirrors into the Grenouille device, which allows for real-time monitoring of the pulse width and other beam characteristics. Similarly, the working characteristics of the RegA were displayed on an oscilloscope, which was used to tune the injection and ejection phases of the pulses in the amplifier. As shown in Figure 8,

there was an "optimum" display of these settings which provided the shortest-duration pulses as measured by the Grenouille, while also providing the highest power in the beam. This power was measured with a standard Coherent power meter at a point just after the first turning mirror (after compressor) in the laser system. By using these diagnostic instruments, it was possible to consistently tune the laser so that each experiment could be carried out in a repeatable fashion.
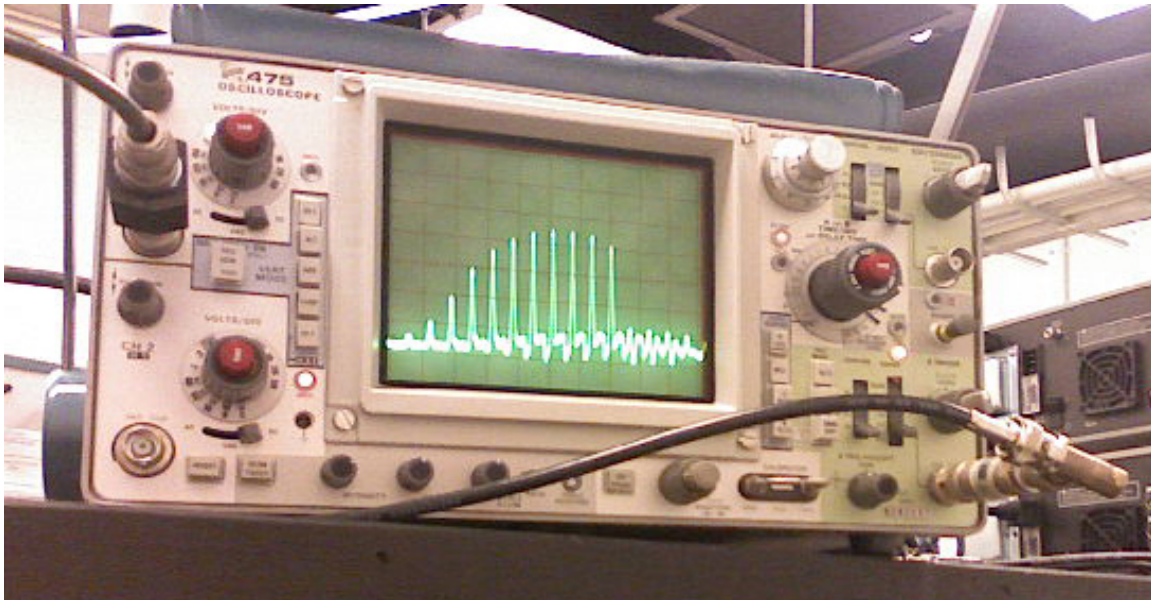

Figure 8. Photo of oscilloscope showing diagnostic output from RegA

As calculated previously, the laser system used in this research effort is capable of producing plasma in ambient air. The easiest method is to choose a lens in agreement with equations (2.12) and (2.13), aligned so the beam passes through lens center, and a visible plasma spark is produced in ambient air. However, when two steering mirrors, an adjustable neutral density filter, and an SHG crystal are added to the system, the plasma

is too weak to be seen through safety goggles under fluorescent laboratory lights, as shown in Figure 9. Since the overriding concern in laboratory work is the safety of the researchers, the first step in this research was to find a safe method to "see" the plasma spark.
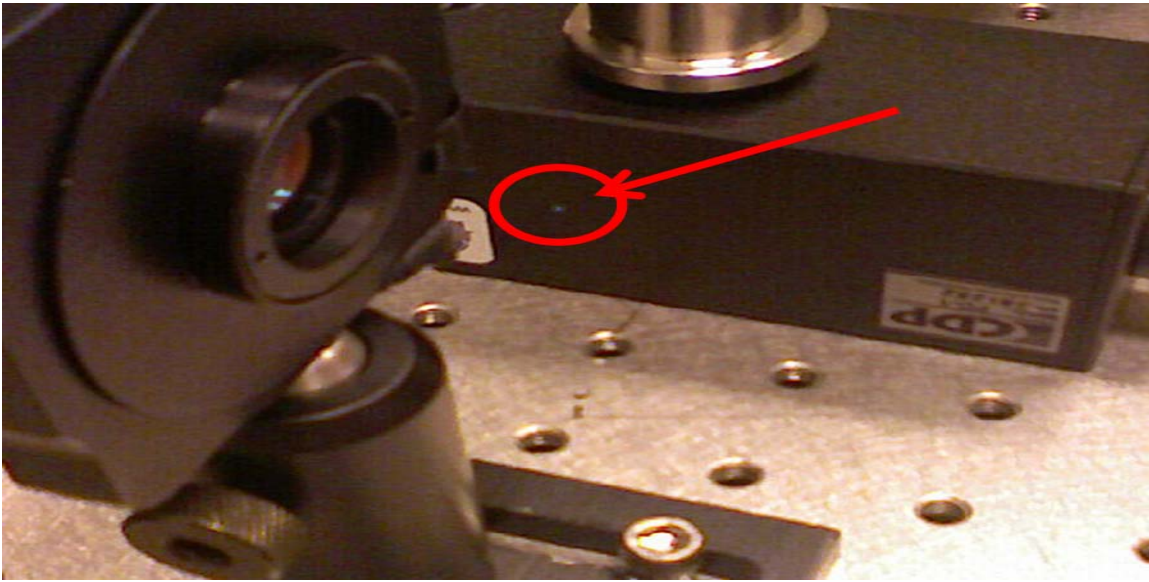

Figure 9. Photo from lab showing achromatic lens and plasma spark

One method of detecting the plasma is to use an insulated coaxial cable as a probe, with one end of the core wire exposed and the connector terminating at the 1MΩ input of a lock-in amplifier, as shown in Figure 10. The plasma ionization of air yields a measurable electromagnetic field due to charge migration in the air molecules. This field causes charge to move in the exposed end of the coaxial cable, resulting in a voltage measured on the lock-in amplifier [18]. Unfortunately, for low density plasmas such as that in ambient air, this method does not give a definitive measure of the strength of the plasma or a reliable on-off determination.
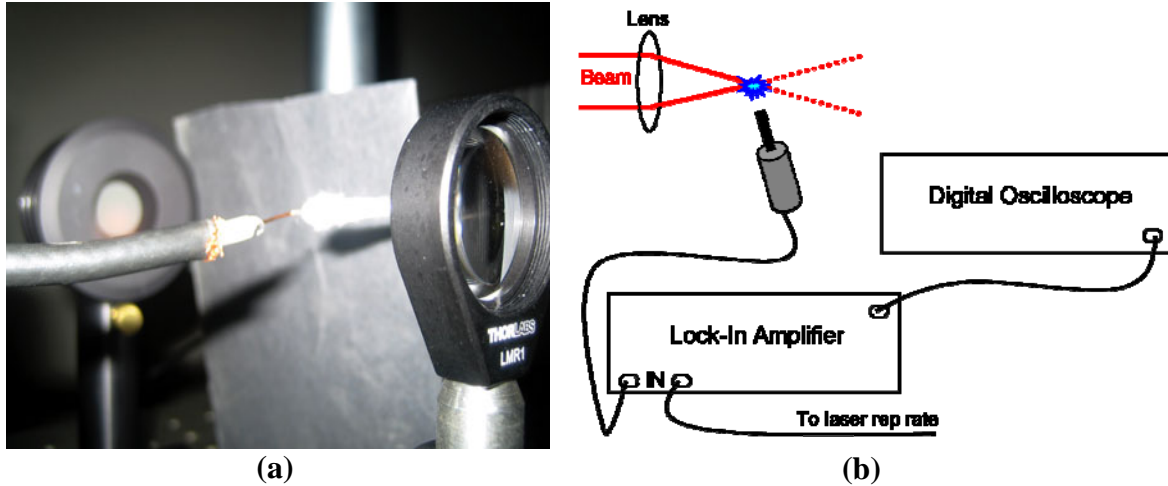
20

<table>
| **(a)** | **(b)** |
</table>

Figure 10. (a) Photo showing coax detector and **(b)** schematic of coax detector setup

The next logical step was to use a photomultiplier tube (PMT) to see the photons produced by the weak plasma. A strong filter is needed at the PMT input to remove the room lights and laser pulse from the signal. Of the filters available, a 3371 Å filter was chosen to allow only the photons from the nitrogen line of the plasma. The chosen filter passes approximately 14.75% of the light at 3371 Å, while blocking nearly 100% outside of this narrow line, as shown in Figure 11. However, even with this filter in place, any plasma signal reaching the PMT was washed out by laser light scattered from the optics and mounts near the plasma location. This is illustrated in Figure 12, where we see the PMT signal is linear with laser power. The third alternative was to use a 40 kHz ultrasonic transducer to "listen" to the popping of the air molecules as the plasma is created. As shown in Figure 13, the transducer is input to a lock-in amplifier keyed to the laser repetition rate, and so the lock-in signal is due to the plasma created by the laser. Figure 14 clearly shows that the transducer can hear the plasma turn on, and the transducer signal provides a reliable proxy for plasma strength, while the PMT signal

21

remains linear with laser power. Thus the transducer makes an effective plasma field

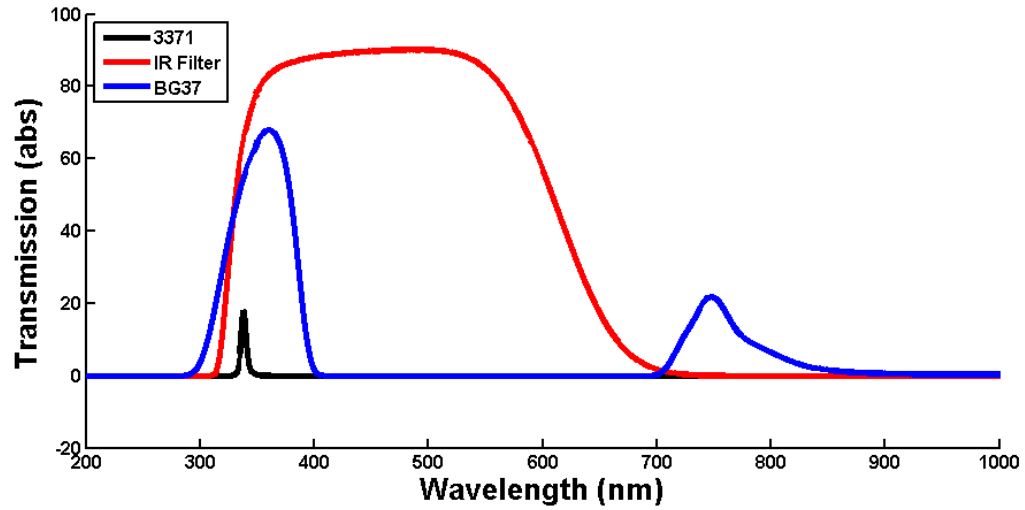intensity detector, and detects the plasma turn-on threshold.
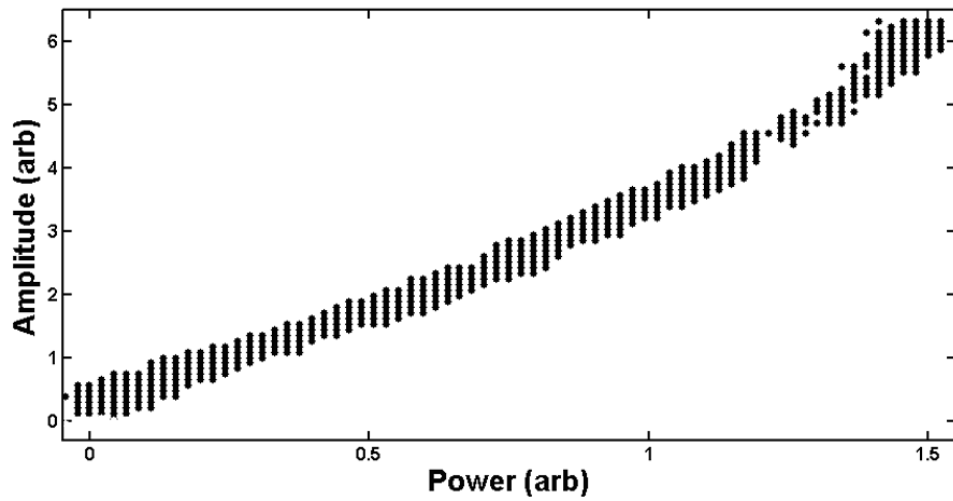

Figure 11. PMT filter performance comparison

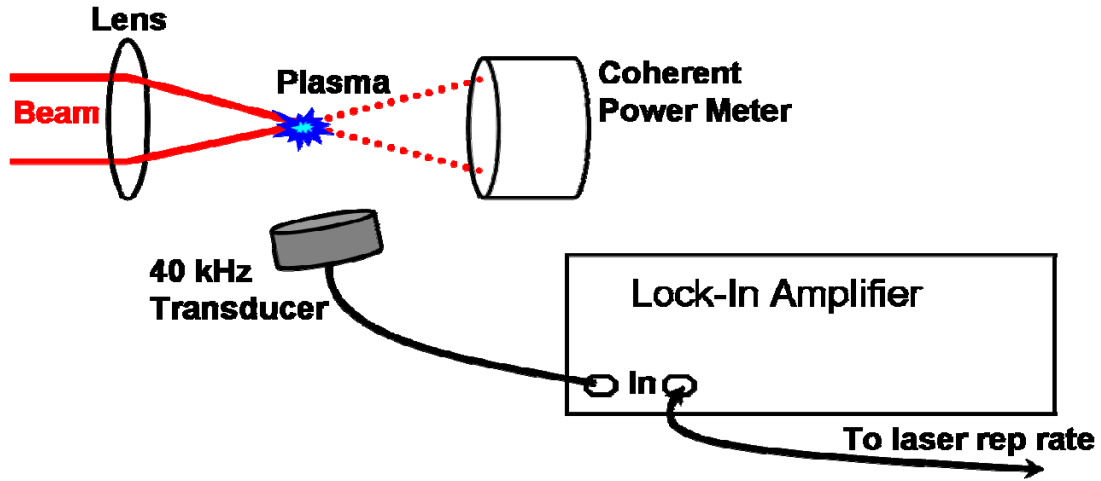**Figure 12.** PMT plasma detection signal as function of laser power

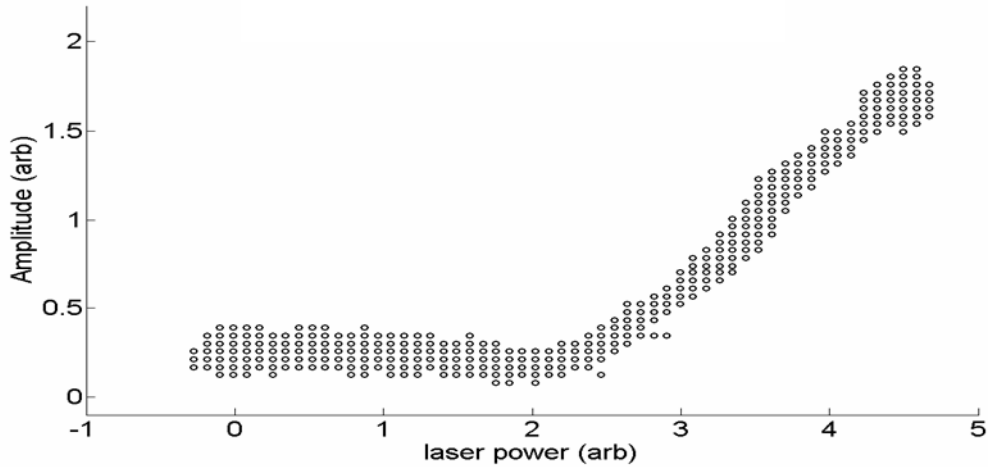**Figure 13.** Schematic of 40kHz ultrasonic transducer as plasma detector

Figure 14. Transducer plasma detection signal as function of laser power

Once this safe method of plasma detection was verified, research into optimizing

the plasma signal, blue light production, and THz generation could proceed. The setup

was modified by placing the SHG crystal after the focusing lens, as shown in Figure 15.

With the SHG in place, a neutral density filter (NDF) must be used at some point before

the SHG crystal. The BBO (β-BaB2O4) crystal has a damage threshold of between 7 and

10 GW/cm^2 [19], and therefore can be easily damaged if the full power IR beam is focused into it. It should be noted that while the laser system was typically very stable, even very small fluctuations in power output resulted in relatively large fluctuations in the plasma intensity. This behavior is illustrated in Figure 16.
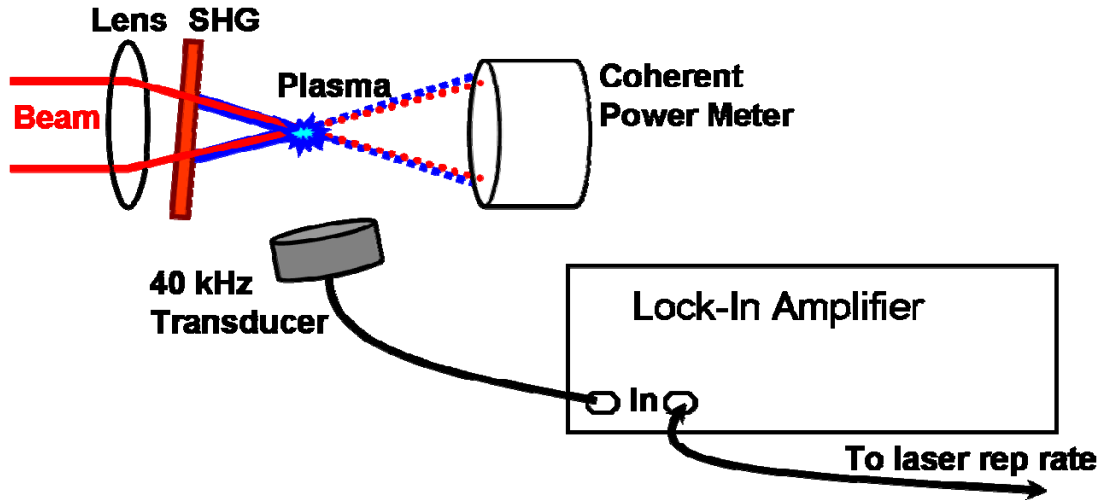

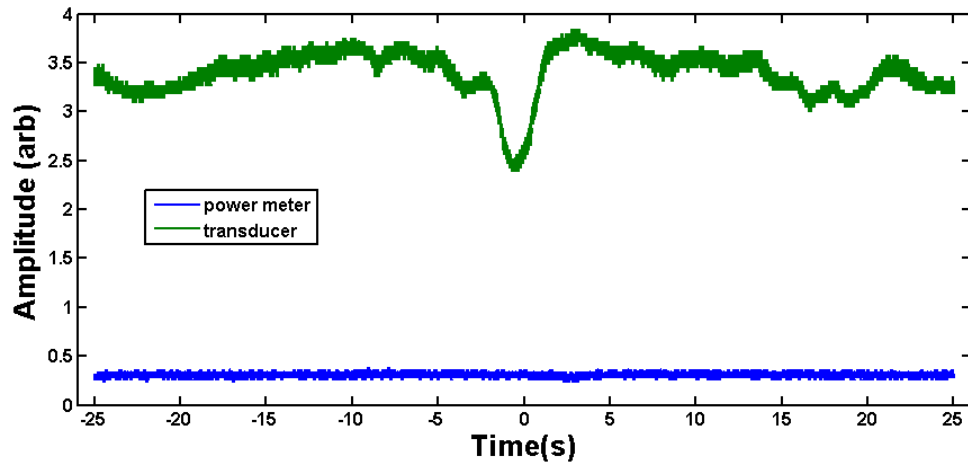**Figure 15.** Schematic of setup with SHG crystal

Figure 16. Typical plot of transducer plasma signal vs. beam power

We have seen that the pulse width is related to the chirp of the pulse, and in this laser system the chirp can be controlled via a manual adjustment on the stretcher/ compressor component, which can also be described as a grating GVD compensator. The actual laboratory mechanism is shown in Figure 17. Adjustment to the physical separation of the gratings results in a linear temporal chirp in the pulse. As described earlier, a chirp in frequency causes a spread in bandwidth with no change in temporal pulse width. Here, the chirp in temporal phase results in the pulse spreading in time, with no change in the frequency spectrum. Although this adjustment did not allow for quantitative measurement of the pulse chirp, the pulse width can be seen real-time with the Grenouille, and Figure 18 shows a clear relationship between the pulse width and the plasma signal. In Figure 18, the pulse width started out at 47 fs (-50 seconds on plot), and was slowly increased to about 65 fs. The dashed red line points out the peak plasma signal at a pulse width of 55 fs, while the large dip at 15 seconds was due to a power fluctuation in the laser itself. All pulse widths were measured by the Grenouille. We know that positive GVD in the optics will cause the pulse to spread apart in the time domain. The behavior shown in Figure 18 demonstrates that by pre-chirping the pulse, we can compensate for the dispersion in the optics, allowing the pulse to arrive at the focal point of the lens (the plasma location) with its minimum in temporal width, and therefore its peak energy [20].
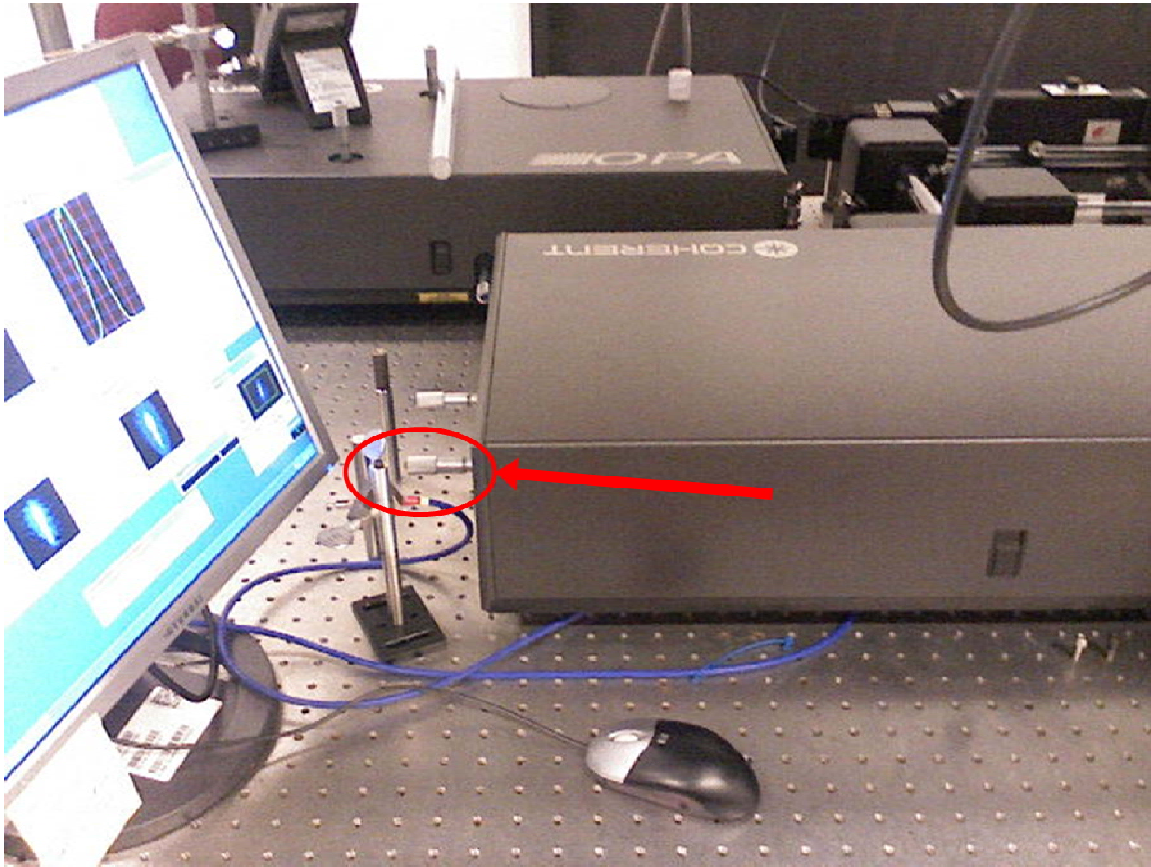
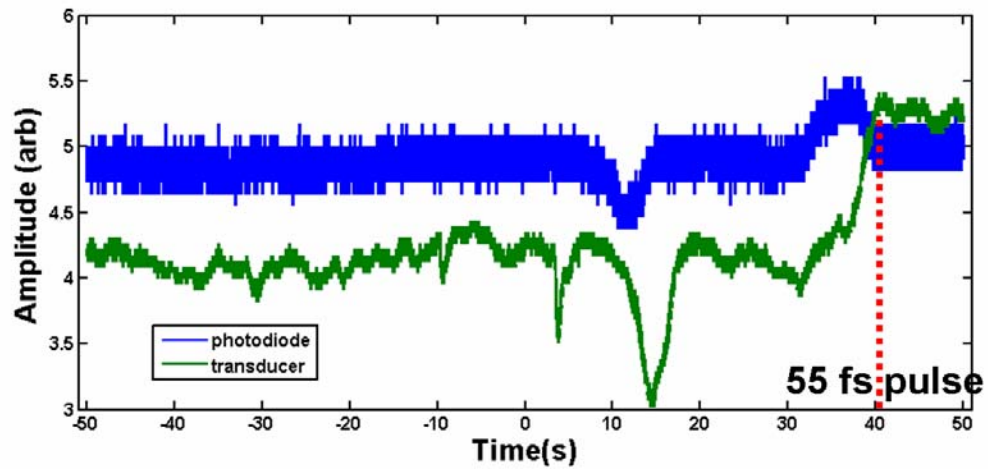**Figure 17.** Mechanism to manually adjust width of pulse exiting compressor

Figure 18. Effect of pulse width on laser power and plasma signal

The next logical step was to optimize the blue light produced by the SHG crystal. To begin with, optimal orientation of the SHG crystal was determined by carefully measuring blue light power as the crystal was aligned. Optimal alignment, defined as peak blue light power, was achieved with rotation of the crystal to 101.5 and 281.5 degrees as marked on the crystal mount. These figures are relative, however, as there was no correlation between mount "zero" rotation and the physical crystal axes.

The optimal crystal rotation about the z-axis was also chosen by looking for the peak of blue light power, and this peak occurred with the crystal aligned approximately 3 degrees off vertical. Once this alignment was achieved, the power of blue light produced then depends solely on the SHG crystal's distance from the focal point of the lens. The closer the crystal is to the focus, the more blue light power produced, as illustrated in Figure 19. Note that the travel of the crystal is stopped prior to the lens focal point to avoid crystal damage; even at very low power, placing the crystal at the focal point results in damage to the crystal. Also, as noted earlier, care must be taken not to allow too much IR power past the NDF. If too much IR (beam) power passes through the focusing lens, the crystal will be damaged.
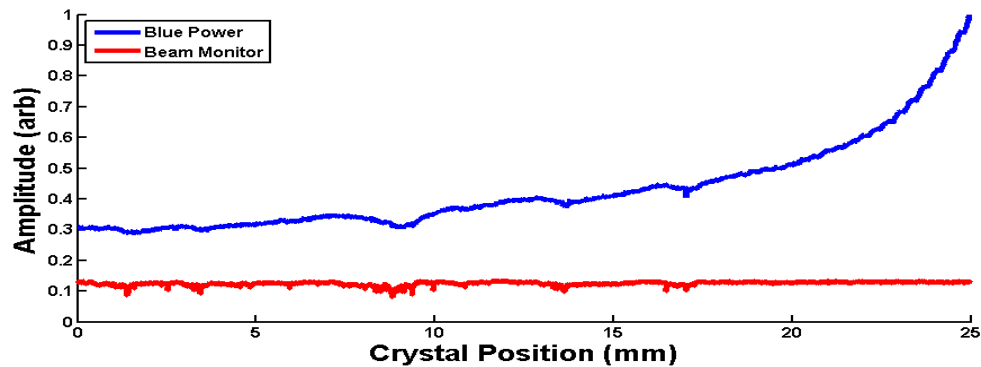

Figure 19. Blue light intensity vs. crystal position

With the SHG crystal characteristics well defined, it was time to look for the THz being created within the plasma via the four-wave mixing process. A Microtech pyroelectric (LiTaO3-based) THz detector was placed behind a Microtech THz-pass filter in the beam path line after the plasma spark. The THz-pass filter transmits 80% from .1 to 3 THz [21]. Unfortunately, at this point no THz was detected, as can be seen in Figure 20. Similarly, Figure 21 clearly shows that when the beam is blocked, the signals from the photodiode power meter and the transducer plasma monitor both drop to zero, while the signal from the THz detector is unaffected. Therefore, while FWM within the plasma should theoretically be producing THz, the THz power is below what the pyroelectric THz detector can detect. The THz detector has a noise-equivalent power of $10^{-8} \dfrac{W}{\sqrt{Hz}}$ at 20 Hz modulation. We can use this figure to calculate the upper limit on the power of the
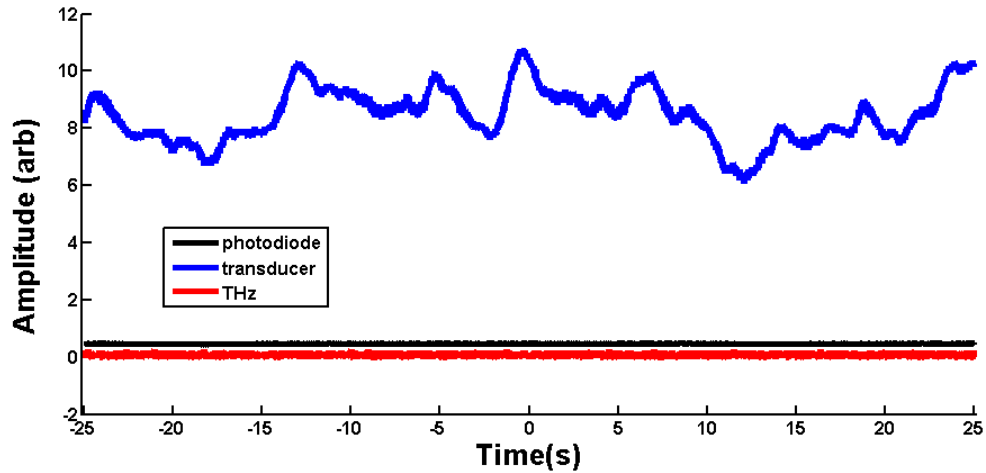

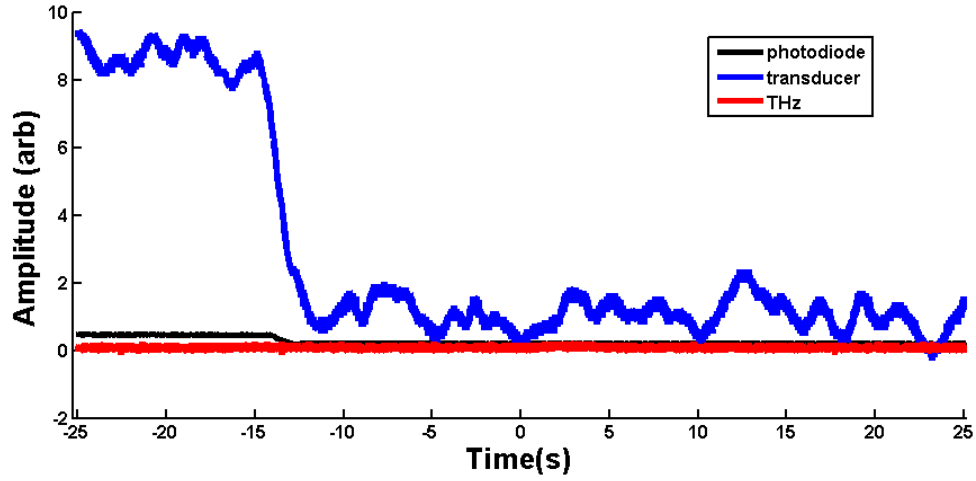**Figure 20.** THz not detected despite good plasma signal

28

Figure 21. Confirmation that THz detector sees no THz from plasma

THz radiation produced by the plasma using Equation (4.1):

$$\frac{P_{source}}{4\pi r^2} = \frac{P_{det}}{A_d}$$ (4.1)

where P_{source} is the power of the THz radiation, P_{det} is the threshold power of the detector, r is the distance from source to detector, and A_d is the area of the detector. This calculation is made with the assumption that the plasma radiates THz as a point source. For this research, the integration time of the lock-in amplifier was typically 1 second, giving $P_{det} = \sqrt{1/1s} \cdot 10^{-8} \frac{W}{\sqrt{Hz}} = 1 \cdot 10^{-8} W$ as the power threshold of the detector. The area of the detector was measured to be $\pi(.25cm)^2$, and the detector was 10 cm from the plasma. Plugging everything into Equation (4.1) and solving for P_{source} yields a power value of $6.4 \cdot 10^{-5} W$. Recalling that the THz filter transmits approximately 80% of the THz power, we arrive at 80 µW as a maximum value for the THz power produced from the plasma (or a minimum detectable power). This would be a good time to give some

thought to how much THz power we expect to see from the plasma we are producing. We know the average power of the IR beam is 750 mW. We can assume that the FWM process in the plasma produces one THz photon for every blue photon that arrives in the plasma, giving a quantum efficiency of
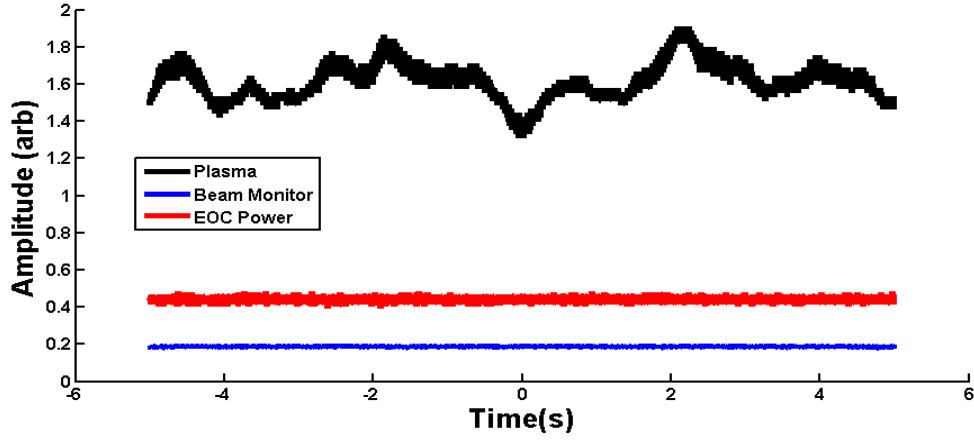
$$\eta_q = \frac{\lambda_{Blue}}{\lambda_{THz}} \tag{4.2}$$

Assuming the plasma is producing photons at 1 THz frequency ($\lambda = 300\mu m$), Equation (4.2) gives a quantum efficiency of $1.33 \cdot 10^{-3}$. The maximum power of THz produced via FWM in the plasma is given by

$$P_{AVG} \cdot \eta_{Blue} \cdot \eta_q = MaxP_{THz} \tag{4.3}$$

Lab measurements with the laser producing P_{AVG} of 674 ± 5 mW recorded an average Blue power of 120 ± 1 mW, using the Coherent power meter and an IR filter. The IR filter, as shown earlier in Figure 11, transmits 88.26% at 400 nm, giving an efficiency of $\eta_{Blue} = 20.2\%$ to create blue photons with the SHG crystal. Combining all these figures into Equation (4.3), we have a value of 0.2 mW for the maximum THz power produced. At first glance, we should easily detect this level of THz power with the pyroelectric detector. However, we have seen that very small laser power fluctuations have large impact on plasma signal, and we were assuming 100% conversion of blue photons to THz photons. We also assumed THz production at 1 THz; if production is at .1 THz our quantum efficiency is reduced by a factor of 10. It becomes easy to imagine how we could be producing much less than the maximum calculated.

Given the undetectable THz power output from the plasma, the search for a THz signal was postponed while the relationship between crystal location, blue light power

30

and plasma signal strength was investigated. Previous publications have reported THz yield intensities that vary sinusoidally with the distance from crystal location to plasma [22, 23]. Therefore it is expected that the plasma intensity will also vary sinusoidally with crystal location. However, as Figure 23 and Figure 24 show, although the plasma intensity increased with the crystal's proximity to the focal point of the lens, the increase was not a smooth function. Instead, it resembles an increasing exponential with a periodic modulation. Regular or not, this seemingly strange function of plasma intensity was highly repeatable under varied conditions using two separate methods.

The first method consisted of manually stepping through 25 mm, while taking ten seconds of data at each 1 mm interval, as shown in Figure 22. The power-versus-time data were then averaged over the 10 seconds to produce one power-versus-position data point, with a typical 25 mm result presented in Figure 23. In the following plots, "EOC" refers to "End-Of-Chain", meaning that the EOC detector was at the end of the optical train.

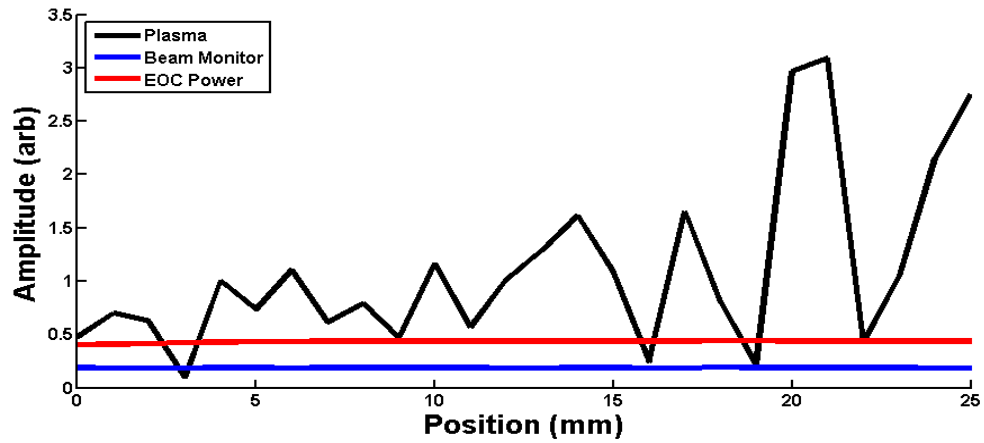**Figure 22.** 10-second power vs. time data taken at each 1 mm step over 25 mm

Figure 23. Plasma intensity vs. crystal position produced from 25 steps
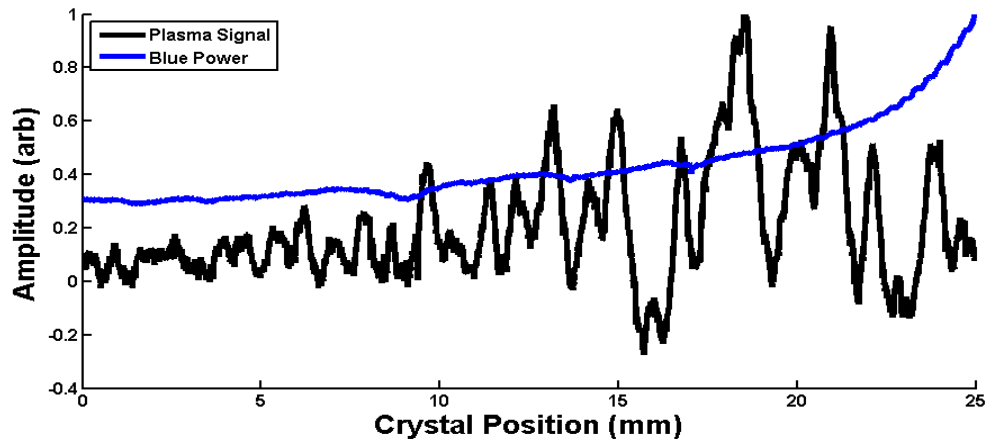

Figure 24. Blue light intensity and plasma signal vs. crystal position

The second method consisted of a stepper motor driving the crystal mount through the 25 mm while the data was acquired by computer through an A-to-D board at a user-controlled step size. The results of this method are presented in Figure 24, showing agreement with the results of the first method. While repeatable, the vast discrepancy between this data and the results both expected and previously published warranted further investigation. Two more datasets were collected, one with the empty crystal

32

mount translated across 25 mm, and another with the mount itself removed while the

translation stage was moved through the 25 mm, as shown in Figure 25 and Figure 26. As

shown in Figure 25, the repeatable structure of the transducer signal is due not to a

changing intensity of the plasma field, but rather to acoustic reflections from the crystal
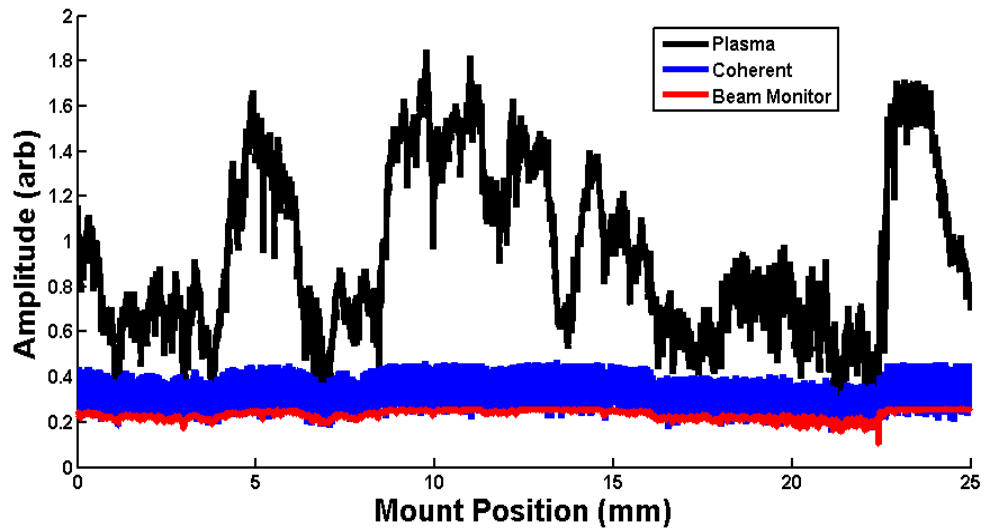
mount itself.

Figure 25. Plasma signal intensity vs. position of empty crystal mount
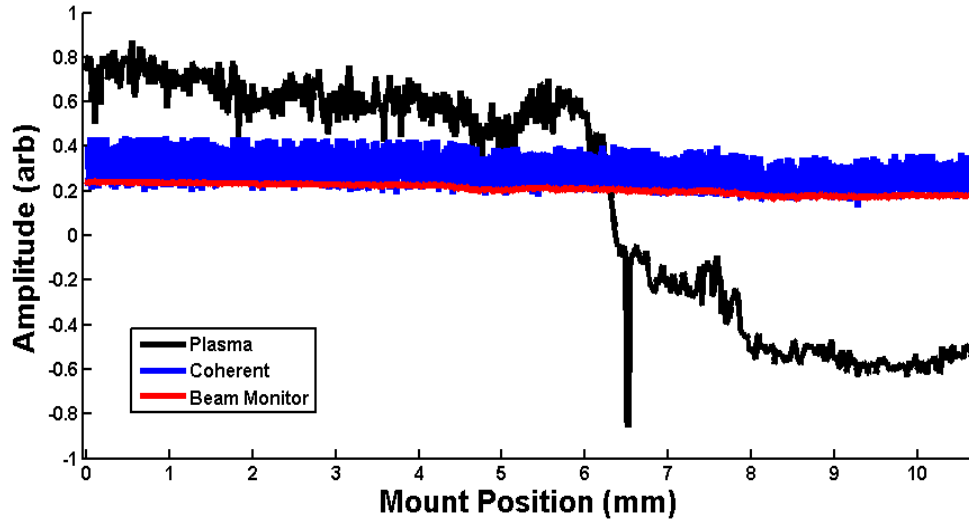
Figure 26. Plasma signal intensity vs. position of empty translation stage

Note that Figure 26 also shows plasma cutoff as the laser power drops below the
threshold for plasma production.

While disappointing, this discovery led to a different method of producing
plasma. Instead of one focusing lens, a beam expander was added to the system, with the
SHG crystal placed inside the beam expander as shown in Figure 27. In this setup, the
crystal is placed such that 0 mm corresponds to the location of the crystal's upstream
face, positioned approximately 1mm downstream of the focal point of the first lens in the
beam expander. Thus the blue light intensity decreases as the x-position increases from 0
to 25 mm. Previous research indicates that a beam expanded to approximately ¼ to ½ the
diameter of the focusing lens produces the most intense plasma field [24, 25]. In this
research, we use L1=125 mm and L2=300 mm, expanding the beam to approximately 6.5
mm prior to the 12 mm (diameter) achromatic focusing lens (f = 25 mm). Repeating the
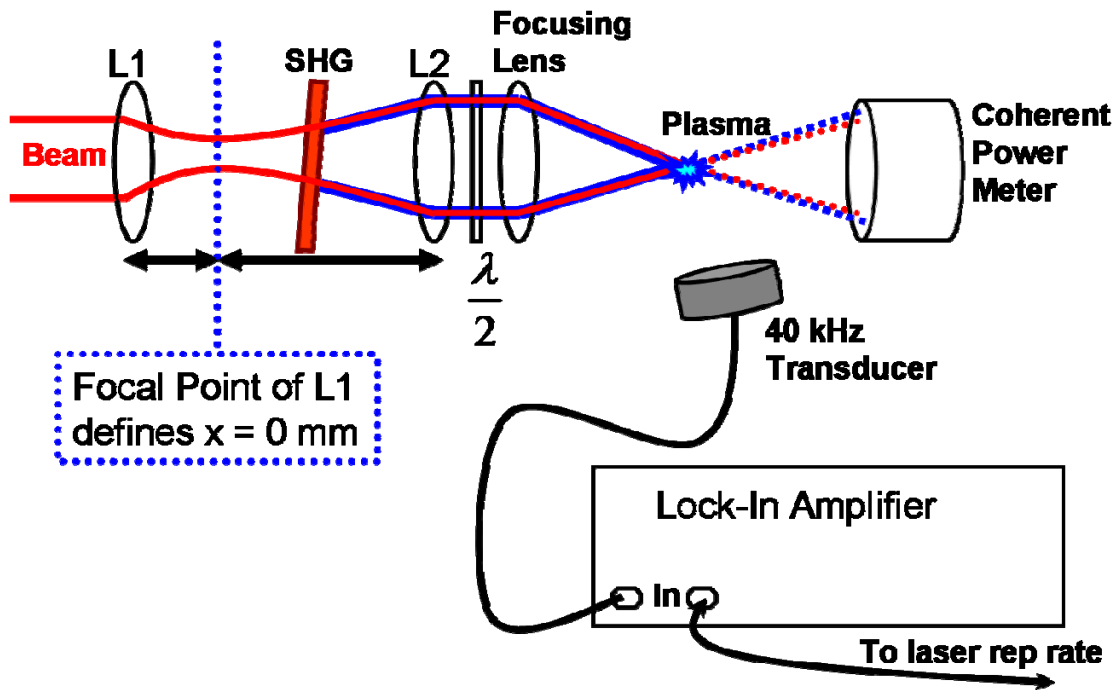
34

Figure 27. Optical train setup with SHG crystal inside of beam expander

power density calculation of section 2.2 yields a power density of approximately 1.5×10^{15} W/cm^2 at the focal point of the lens, which is an order of magnitude stronger than the earlier value. With the crystal inside of the beam expander, there are no moving parts in the vicinity of the transducer, thereby eliminating the acoustic reflections. As advertised, the plasma spark was now visible to the goggled eye with the room lights on, marking a significant increase in plasma field intensity. Encouraged by this result, the THz detector and Microtech filter were put back in place of the Coherent power meter and the search for THz resumed. Unfortunately, as can be seen in Figure 28, the THz detector was again unable to see any THz from the plasma. Similarly, as with earlier results, Figure 29 clearly shows that while the transducer sees the plasma turn off and on as the beam is blocked and unblocked, the THz signal is unchanged.
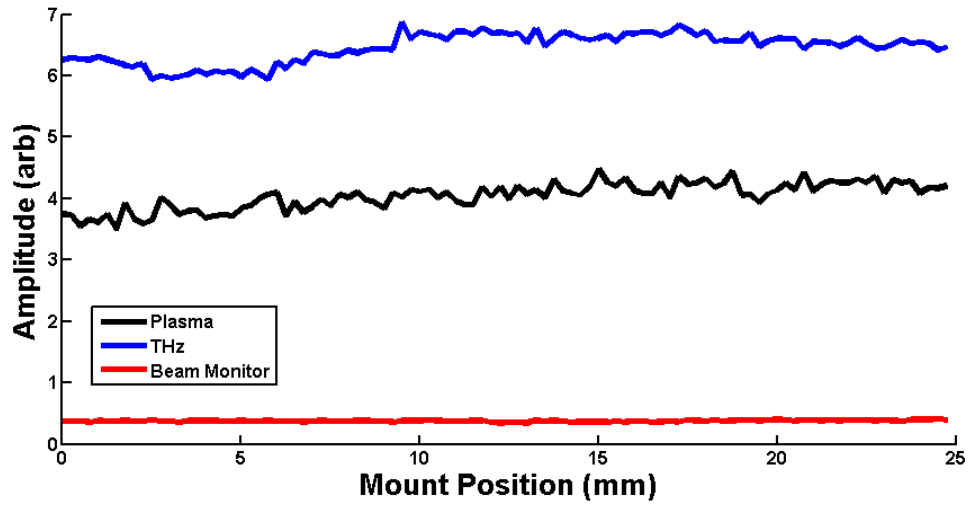
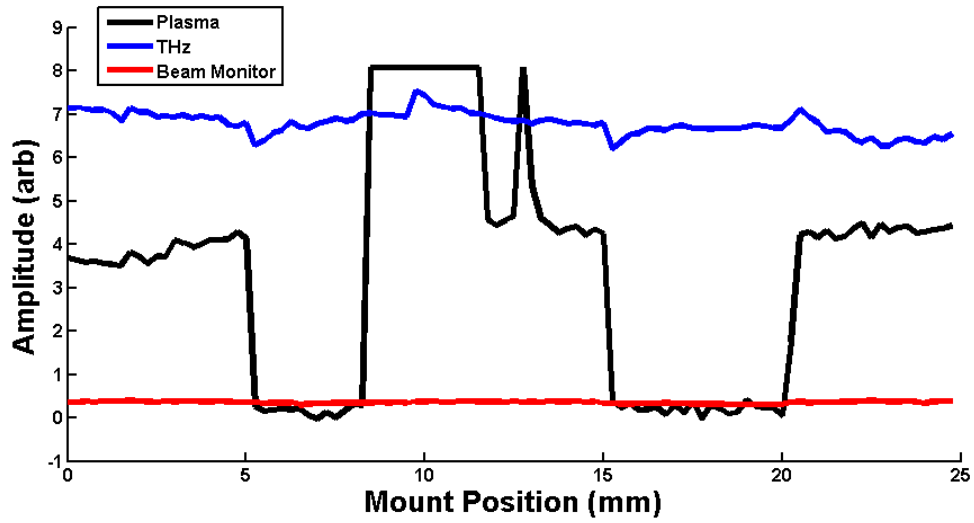**Figure 28.** Terahertz detector signal vs. crystal position

Figure 29. No change in THz detector signal with plasma on-off

Returning to the characterization of the crystal and optics, it was verified that the crystal was still producing a sufficiently intense blue light from inside the beam expander. As expected, and shown in Figure 30, the blue light intensity is still proportional to the crystal's distance from the focal point of the lens.
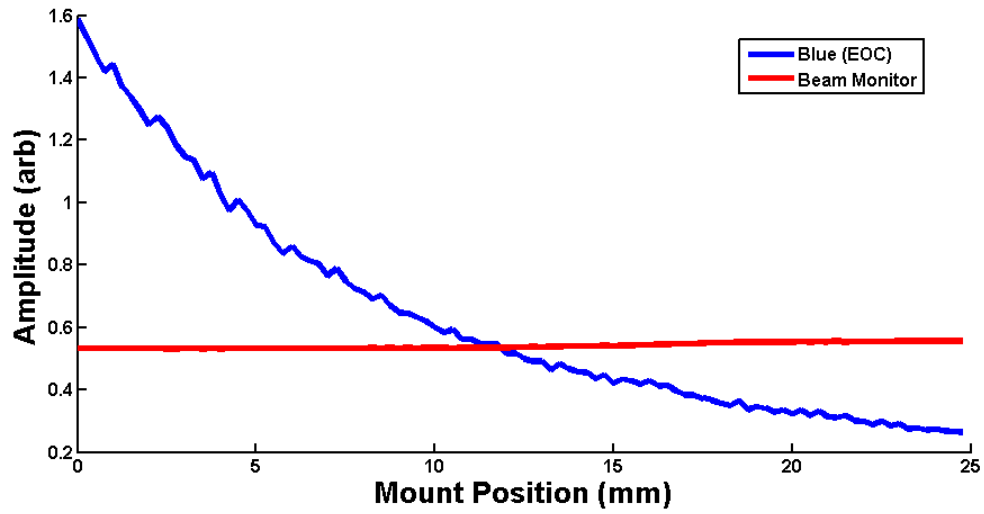
36

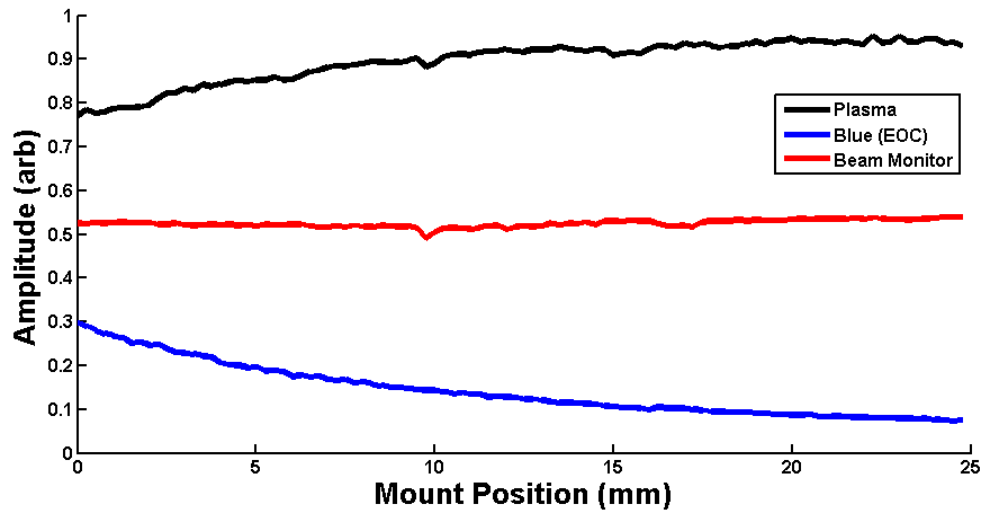**Figure 30.** Blue light intensity vs. crystal position

Figure 31. Plasma signal vs. blue light intensity

Surprisingly, the plasma intensity decreased as the blue intensity increased, as seen in Figure 31. When looking at the total power, however, we see that the plasma intensity and total power increase or decrease together as shown in Figure 32. Also in apparent contradiction to Figure 31, Figure 33 shows the effect of crystal rotation on blue

37

intensity and plasma intensity, showing that as blue power increases, so does plasma intensity.
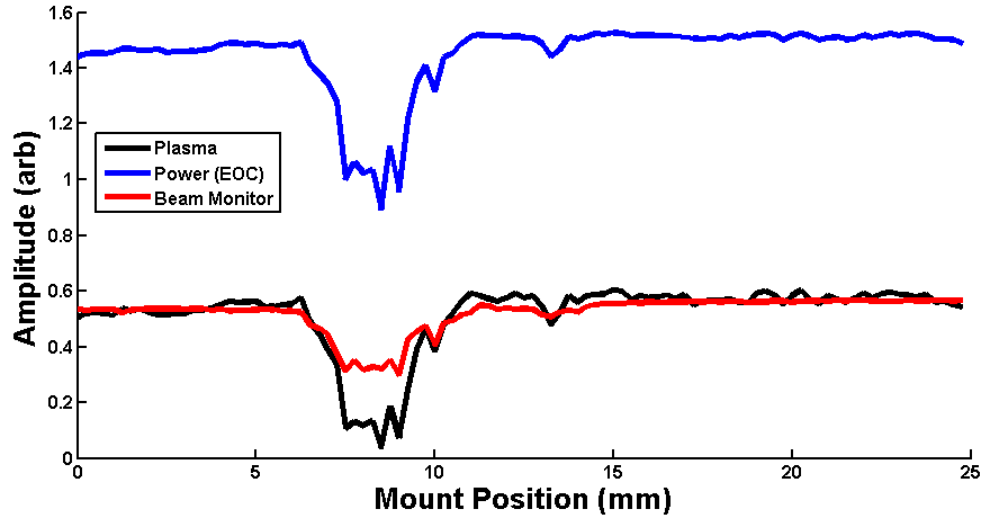

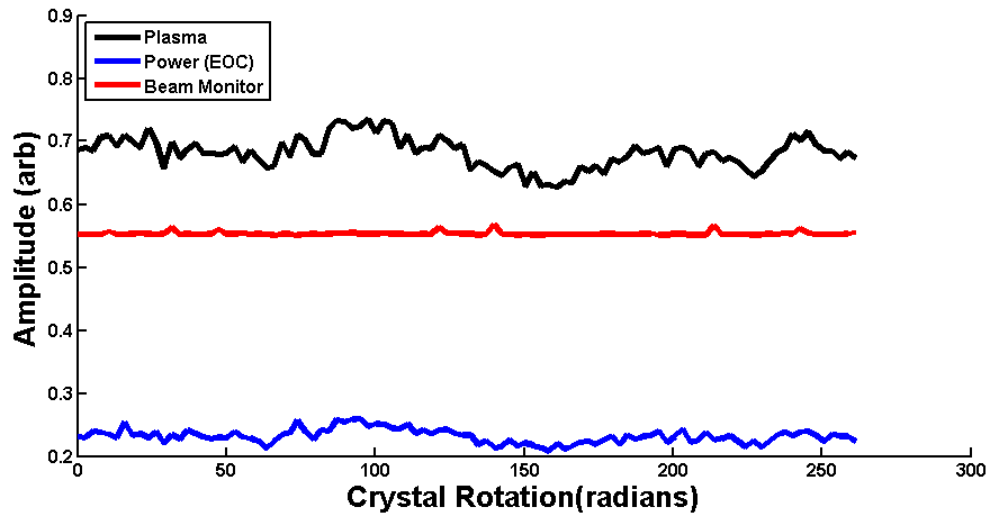**Figure 32.** Plasma signal vs. total (IR + Blue) intensity

Figure 33. Plasma signal vs. Blue light intensity

The solution to this apparent discrepancy lies in a closer look at the system setup for these different data sets, and some thought on the nature of the SHG crystal. The

setup for the earlier data did not include a λ/2 (for 800 nm) waveplate, while the rotation setup did. We know that the IR beam from the laser is horizontally polarized. The SHG crystal is a type I BBO, which means that the crystal has an EEO axis format. There are two orientations that produce a blue light peak, one at each E axis. These peaks occur at 101.5 and 281.5 degrees on the rotating mount. Aligning the crystal along either of these axes produces blue light that is vertically polarized. Without the λ/2 waveplate, the blue light and the IR beam are polarized perpendicular to one another at the focal point of the lens, and so do not add coherently to the plasma intensity, although they do both add to the total power. This explains the result of Figure 31 and Figure 32. With the λ/2 waveplate in the system, the blue light and IR beam are both polarized vertically and so they add coherently to plasma production, as seen in Figure 33.

Time constraints allowed one last attempt in the increasingly desperate search for THz radiation. The optical train was completely rearranged to use the electro-optic technique for THz detection, with the initial diagnostic setup as shown in Figure 34. This setup allows for a known THz source to be used to ensure correct alignment of the optical trains and proper calibration of the Nirvana autobalanced photodetector. The key challenge of this technique is that the reference beam path length must be precisely equal to the signal path length. Reference beam path is from beam sampler through mirrors and corner reflector (CR) to pellicle, while signal path is through chopper to ZnTe (which produces THz) through filter and parabolic mirror to pellicle. Signal output of Nirvana is then due solely to presence of THz signal at the chopper modulation frequency. For this
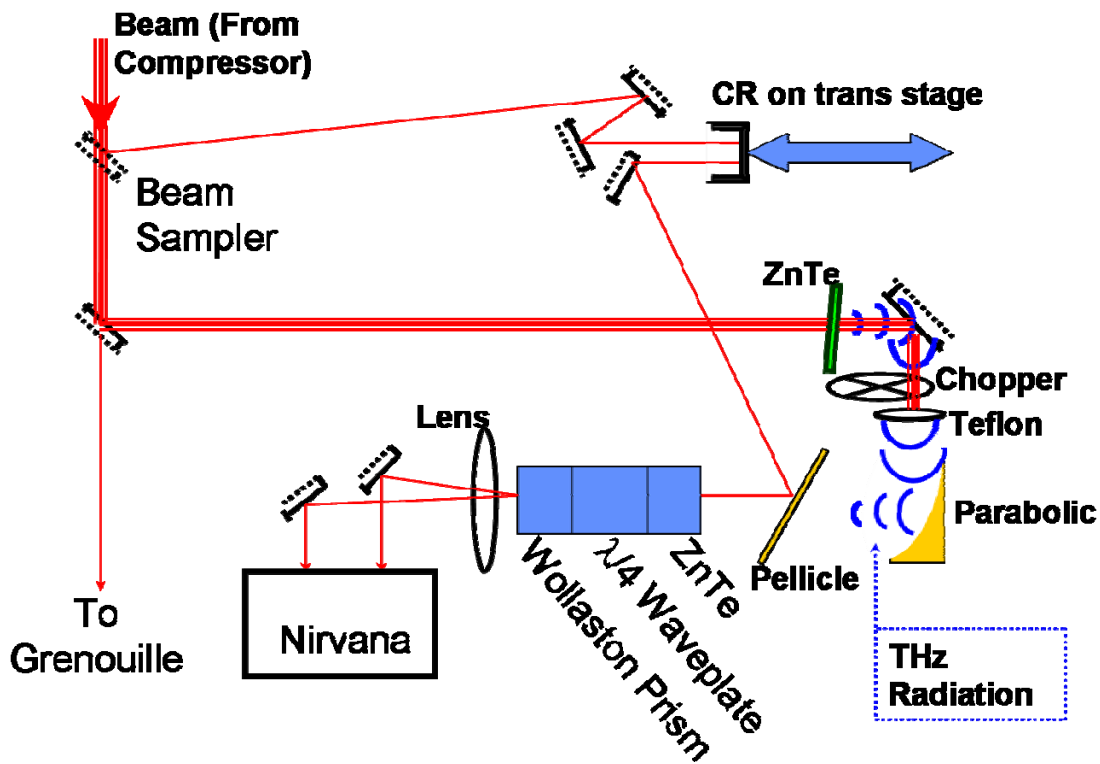
Figure 34. Schematic for electro-optic THz detection

method to detect THz, the two beams must overlap in both time and space at the pellicle

and at the ZnTe (detection) crystal in order for the Nirvana to be able to detect a signal.

There is added complexity here because the corner reflector is on a translation stage.

Thus the beams must remain in alignment as the corner reflector is moved back and forth.

As shown in Figure 35, using the ZnTe to produce THz, this setup does indeed detect

THz when the beam paths are of equal length (zero delay). As the corner reflector is

scanned through some distance (in this case 23 mm), we see the THz signal peak at the

zero delay point. The scan distance in mm is converted to time in picoseconds simply by

dividing by the speed of light and converting units. Figure 36 shows the same data in

frequency space, giving a bandwidth of approximately 2.7 THz for this detection method. The deep spikes in the frequency-space spectrum are due to the absorption of THz by water vapor in air.
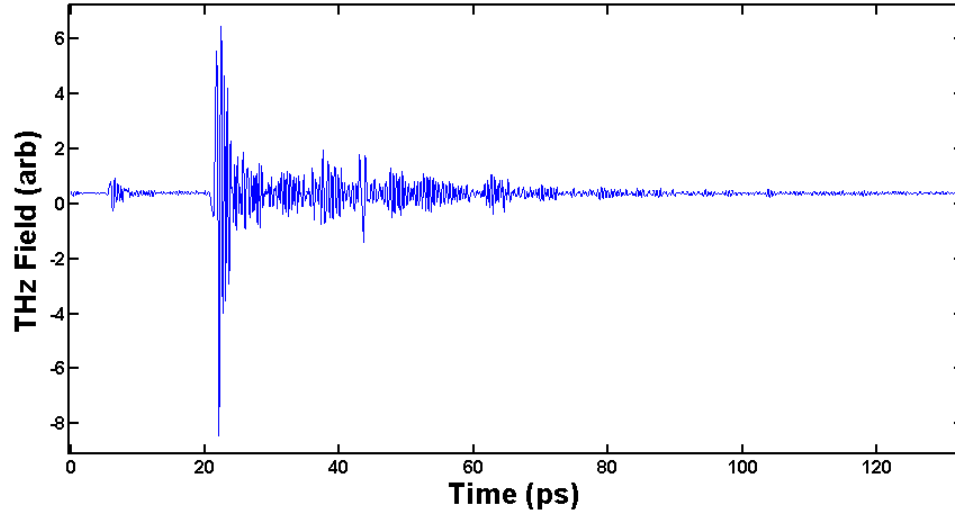

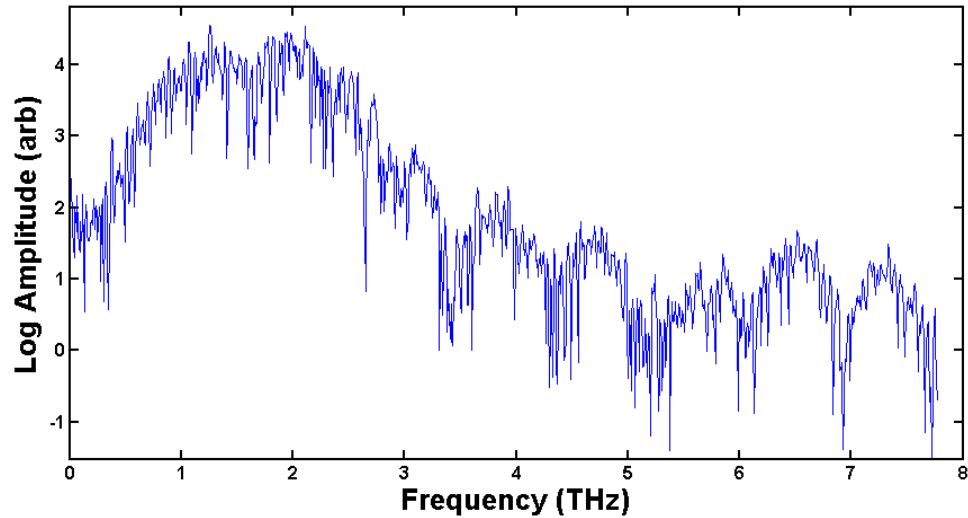**Figure 35.** EO Detection of diagnostic THz signal (time domain)

Figure 36. EO Detection of diagnostic THz signal (frequency domain)

One explanation for the very low power of THz produced may lie in the way in which the THz is amplified in the plasma. Once the THz is produced via FWM, we can assume that the power grows as a small signal, i.e. as $e^{\alpha x}$, where x is the propagation length through the plasma. Making the further assumption that the size of the plasma is roughly equal to the Rayleigh range of the beam after the focusing lens, we can calculate the length of the plasma filament that lets the THz signal grow. For this research,

$w_0 = \dfrac{1.22 f \lambda}{2d}$, and the Rayleigh range is given by $\pi w_0^2 / \lambda$, yielding a Rayleigh range of

80 μm. Comparable published research had Rayleigh ranges from as low as 74 μm [22] to as much as 7.4 mm [22], as shown in Table 1. The Rayleigh Range argument appears to be a good explanation for the difference in THz power produced during this research and the power figures presented in related publications. Another explanation also exists for the low THz power produced in this research. The fundamental and second harmonic beams were focused through an achromatic lens to create the plasma in air, while FWM is the process believed to generate the THz. The achromatic lenses used were designed for the IR wavelength (800 nm); it is possible that the focal point for 400 nm blue is far enough away from the expected position that FWM does not actually take place or takes place at a very low efficiency. A remedy for this situation would be to use high quality curved focusing mirrors instead of achromatic lenses. This change would eliminate chromatic aberrations, although curved mirrors do introduce astigmatism into the beam.

The next logical step is to replace the ZnTe crystal with the beam expander, SHG crystal and focusing lens to produce THz from laser-generated air plasma, and see if the

EO setup can detect the signal. While this step would provide a nice completion to this

research, time constraints did not allow the attempt.

Table 1. Comparison to similar research

Beam Dia. (mm)	f (mm)	z0 (μm)	Peak pulse energy	Pulse Width (fs)	Plasma Power Density (x 10^{14} W/cm^2)	THz Power (W/cm^{2}s)	Ref
2.7	25	80	8 μJ	50	2.5	undetected	This Thesis
6.5	25	14	8 μJ	50	14	undetected	This Thesis
8	150	335	25 mJ	200	460	$6 \cdot 10^7$	[22]
4*	50	146	.5 mJ	25	170	$4.25 \cdot 10^8$	[26]
**	200	884	860 mJ	140	87	unspecified	[27]
5.6	50	74	460 mJ	140	91	unspecified	[28]
"	200	1185	"	"	5.7	"	[28]
"	300	2670	"	"	2.5	"	[28]
"	500	7410	"	"	.91	"	[28]
* If beam diameter was unspecified, 4 mm was assumed for calculations							
** Spot size was specified							

CONCLUSION

All the groundwork has been laid for a next attempt at detecting THz from laser-induced air plasma. Detection methods for "hearing" the plasma with an ultrasonic transducer were introduced, and the plasma itself has been well characterized, as well as the blue light produced by the SHG crystal. The beam expander configuration, crystal alignment, and detection method have all been established. Zero-delay for the EO detection setup has been located, and the diagnostic THz signal has been seen and characterized. Explanations have been put forth to explain the low power of THz produced by laser-induced air plasma in this research, and an upper limit has been determined for the THz power. In addition, valuable experience has been gained in the care and feeding of a femtosecond-pulsed laser system. Time permitting, the next step in the research is to use the beam expander/SHG/focusing lens combination as a THz source through FWM in air plasma, along with using focusing mirrors instead of achromatic lenses.

BIBLIOGRAPHY

1. Federico, J. F., et al, "THz imaging and sensing for security applications – explosives, weapons and drugs," Semicond. Sci. Technol., Vol. 20, S266-S280 (2005)

2. Hargrove, L. E., Fork, R. L., and Pollack, M. A., "Locking of He-Ne laser modes induced by synchronous intracavity modulation," Appl. Phys. Lett. 5, 4–5 (1964)

3. Fork, R. L., Brito-Cruz, C. H., Becker, P. C. and Shank, C. V., "Compression of optical pulses to six femtoseconds by using cubic phase compensation," Opt. Lett. 12, 483–485 (1987).

4. Kukura, P., McCamant, D. W., Yoon, S., Wandschneider, D. B., and Mathies, R. A., "Structural Observation of the Primary Isomerization in Vision with Femtosecond-Stimulated Raman," Science 310, 1006-1009 (2005)

5. URL: http://www.zomega-terahertz.com

6. Diels, J.-C. and Rudolph, W., *Ultrashort Laser Pulse Phenomena,* Academic Press, 2006

7. Verdeyen, J. T., *Laser Electronics, 3rd Ed.*, Prentice Hall, 1995

8. Saleh, B. E. A., and Teich, M. C., *Fundamentals of Photonics, 2nd Ed.,* Wiley-Interscience, 2007

9. Yariv, A., and Yeh, P., *Optical Waves in Crystals,* Wiley-Interscience, 2003

10. Federici, J. F., "Review of four-wave mixing and phase conjugation in plasmas," IEEE Transactions on Plasma Science Vol. 19, No. 4 (1991)

11. Cook, D. J. and Hochstrasser, R. M., "Intense terahertz pulses by four-wave rectification in air," Optics Letters, Vol. 25, No. 16 (2000)

12. Akimov, D. A., *et al,* "Application of coherent four-wave mixing for two-dimensional mapping of the spatial distribution of excited atoms in a laser-produced plasma," Optics Comm. 140, 259-265 (1997)

13. Xie, X., Dai, J., and Zhang, X-C., "Experimental Evidence of Four-Wave-Mixing in THz Wave Generation in Laser Induced Air Plasma," Optical Society of America (2006)

14. Hecht, E., *Optics, 4th Ed.,* Pearson (Addison Wesley), 2002

15. Kane, D. J. and Trebino, R., "Characterization of arbitrary femtosecond pulses using frequency-resolved optical gating," IEEE J. Quantum Electron. 29, 571–579 (1993).

16. Grenouille Model 8-50 User's Guide, Swamp Optics, Atlanta, GA 30339

17. URL: http://www.swampoptics.com

18. Proulx, A., Talebpour, A., Petit, S., Chin, S.P., "Fast pulsed electric field created from the self-generated filament of a femtosecond-pulsed Ti:Sapphire laser pulse in air," Opt. Comm. 174, 305-309 (2000).

19. URL: http://www.bbo-crystal.optical-components.com/bbocrystal-chemicalproperties.htm

20. Muller, M., Squier, J., Wolleschensky, R., Simon, U., Brakenhoff, G. J., "Dispersion pre-compensation of 15 femtosecond optical pulses for high-numerical-aperture objectives," Journal of Microscopy 191 Pt. 2, 141-150 (1998)

21. URL: http://www.mtinstruments.com

22. Kim, K. Y., Glownia, J. H., Taylor, A. J., and Rodriguez, G., "Terahertz emission from ultrafast ionizing air in symmetry-broken laser fields," Opt. Exp. 15 No.8, 4577-4584 (2007)

23. Kress, M., Loffler, T., Eden, S., Thomson, M., and Roskos, H., "Terahertz-pulse generation by photoionization of air with laser pulses composed of both fundamental and second-harmonic waves," Optics Letters Vol. 29, No. 10 (2004)

24. Bors, Zs., and Horváth, Z. L., "How to select a lens for focusing of femtosecond pulses," Brazilian J. of Phys. 26 No.2, 516-519 (1996)

25. Jasapara, J., and Rudolph, W., "Characterization of sub-10-fs pulse focusing with high-numerical-aperture microscope objectives," Optics Letters, Vol. 24, No. 11 (1999)

26. Bartel, T., Gaal, P., Reimann, K., Woerner, M., and Elsaesser, T., " Generation of single-cycle THz transients with high electric-field amplitudes," Optics Letters Vol. 30, No. 20 (2005)

27. Xie, X., Dai, J., and Zhang, X.-C., "Coherent control of THz wave generation in ambient air," Phys. Rev. Lett. Vol. 96, 075005 (2006)

28. Zhong, H., Karpowicz, N., and Zhang, X.-C.,"Terahertz emission profile from laser-induced air plasma," App. Phys. Lett. Vol. 88, 261103 (2006)

1. REPORT DATE *(DD-MM-YYYY)*	2. REPORT TYPE	3. DATES COVERED *(From - To)*
27-03-2008	Master's Thesis	Sep 2006 - Mar 2008

4. TITLE AND SUBTITLE	5a. CONTRACT NUMBER
Production and Characterization of Femtosecond-Laser-Induced Air Plasma	5b. GRANT NUMBER
	5c. PROGRAM ELEMENT NUMBER

6. AUTHOR(S)	5d. PROJECT NUMBER
Armbruster, David R., Capt., USAF	5e. TASK NUMBER
	5f. WORK UNIT NUMBER

7. PERFORMING ORGANIZATION NAME(S) AND ADDRESS(ES)	8. PERFORMING ORGANIZATION REPORT NUMBER
Air Force Institute of Technology Graduate School of Engineering and Management (AFIT/ENP) 2950 Hobson Way, WPAFB, OH 45433-7765	AFIT/GAP/ENP-08-M01

9. SPONSORING/MONITORING AGENCY NAME(S) AND ADDRESS(ES)	10. SPONSOR/MONITOR'S ACRONYM(S)
N/A Intentionally left blank	11. SPONSOR/MONITOR'S REPORT NUMBER(S)

12. DISTRIBUTION/AVAILABILITY STATEMENT
APPROVED FOR PUBLIC RELEASE; DISTRIBUTION UNLIMITED

13. SUPPLEMENTARY NOTES

14. ABSTRACT

The purpose of this research was to produce, characterize, and optimize laser-induced air plasma as a preliminary step in using the plasma as a source of terahertz radiation. An 800 nanometer, 50 femtosecond, 0.75 Watt, pulsed Ti:Sapphire laser system was used as the source infrared beam. A beam expander was used to expand the beam to a diameter of approximately 6.5 mm, and the beam was focused through a 25 mm focal length achromatic lens to produce laser-induced plasma in ambient air. A 40 kHz ultrasonic transducer was used to detect the plasma. A second harmonic generation crystal was placed within the beam expander to generate 400 nm blue light, enabling production of THz in the plasma via four wave mixing; a third-order nonlinear process. While plasma-produced THz was not detected, all the preliminary groundwork was accomplished, including full characterization of the plasma, blue light, and alignment of the system to generate and detect THz. The electro-optic detection apparatus was assembled, aligned and used to successfully detect a diagnostic THz signal.

15. SUBJECT TERMS

Femtosecond Laser, Ultrashort Pulse, Ultrashort Laser, Pulsed Lasers, Plasma, Air Plasma, Terahertz

16. SECURITY CLASSIFICATION OF:			17. LIMITATION OF ABSTRACT	18. NUMBER OF PAGES	19a. NAME OF RESPONSIBLE PERSON
a. REPORT	b. ABSTRACT	c. THIS PAGE	UU	56	Matthew J. Bohn, LtCol., USAF (AFIT/ENP)
U	U	U			19b. TELEPHONE NUMBER *(Include area code)* 937-256-3636 x 4573; matthew.bohn@afit.edu